Scalable 3D Printing of Micro-Optical Elements for Optical Fibres

Mika Seán Mc Keever

Masterarbeit in Physik
angefertigt im Physikalischen Institut

vorgelegt der
Mathematisch-Naturwissenschaftlichen Fakultät
der
Rheinischen Friedrich-Wilhelms-Universität
Bonn

Juni 2024

I hereby declare that this thesis was formulated by myself and that no sources or tools other than those cited were used.

Bonn, 15/6/2024 .... Date

.... Signature

1. Gutachter: Prof. Dr. Stefan Linden
2. Gutachter: Prof. Dr. Sebastian Hofferberth

Contents

CHAPTER 1

Introduction

Since their invention in the mid-20th century, fibre optics have revolutionised data transfer. The first successful data transmission using fibre optics was demonstrated in 1965 [1], marking the beginning of a technological evolution that has become central to telecommunications. The ability of optical fibres to support high bit rate transmission with minimal losses has been key in the development and widespread expansion of the internet [2]. Apart from telecommunications, fibre optics have found applications in fields such as medicine [3], metrology [4], and aerospace engineering [5]. In addition to data transfer, optical fibres are useful tools for their ability to be used, for example, as a waveguide for laser light in optics laboratories or for optical imaging [6]. In medicine, optical imaging fibres are utilised in endoscopes, which can be inserted into the body to provide minimally invasive imaging of internal structures [7, 8]. This use of optical fibres for imaging and light transfer can be combined with a different field of optics: micro-optics.

Micro-optics deals with optical elements typically up to a size of around 2 millimetres [9]. The significance of micro-optics lies in that the optical elements themselves are just two to three orders of magnitude larger than the wavelength of the light passing through them. Various manufacturing techniques exist for producing micro-optics, including ultraprecision machining technologies and Micro-electromechanical Systems (MEMS) [10]. The use of photoresists for the production of micro-optics has been prevalent since the early 1990s [11], particularly through thermal reflow methods [12]. Techniques, such as microdroplet jetting, have proven effective in producing micro-optic arrays quickly and cost-efficiently [13]. 3D printing through direct laser writing via two-photon absorption has enabled the production of free-form micro-optics [14], and the advent of commercially available 3D printing via direct laser writing systems has further facilitated the production of micro-optics in a laboratory setting. This production method is the focus of this thesis.

This thesis explores new methods for the scalable production of micro-optic lenses for use with optical fibres. Using previous work on 3D printed micro-lenses, we improve upon existing printing techniques by moving away from fibre-end 3D printing towards the printing of micro-optical lenses directly onto a substrate. The lenses are then attached to an optical fibre via insertion into a mask that is printed on top. A printing technique is developed that can accommodate various micro-optical lens designs, is scalable in production and allows facilitates attachment to an optical fibre in a plug-and-play fashion.

This thesis is structured in the following format. Chapter 2 gives a theoretical background to the concepts used in the thesis. Chapter 3 explores the printing of micro-structures using a commercially available direct laser writing system for 3D printing. In chapter 4, the design and printing processes for a new optic element used for attaching free-form lenses to optical fibres are discussed. Chapter 5 gives an overview of the experimental characterisation performed on the printed lenses. This is followed by a summary and an outlook on future developments.

CHAPTER 2

Theoretical Background

This chapter provides the theoretical background for understanding the production and experimental methods used in this thesis. First, the theoretical processes necessary for 3D printing via direct laser writing are discussed in terms of light interaction with matter and processes building upon it. Following this, the working principles of optical fibres and collimating lenses are discussed, along with the mathematical description of Gaussian beams.

2.1 Light interaction with matter

This section covers the interaction of electromagnetic (EM) waves with matter. In colloquial language, the word "light" is used to refer to EM radiation that the human eye can observe, whereas, in physics, it is used to refer to EM radiation of any wavelength [15]. It is often advantageous to view light as a stream of light quanta (photons) rather than a wave of EM radiation to explain its interaction with matter.

2.1.1 Single-photon Absorption

Single photon absorption (1PA) is a phenomenon where matter absorbs the energy carried by incident photons. The mechanism of photon absorption can be simplified in the following way. A body (atom, molecule, bound electron, etc.) is in its original (usually ground) state with energy E_0. An arbitrary exited state n has the energy E_n. An incoming photon with its energy E_γ can excite the body from its ground state into its first exited state if the following condition is met:

$$E_\gamma = \hbar\omega = \Delta E = E_n - E_0, \tag{2.1}$$

where $\hbar$ is the reduced Planck constant and ω is the photons angular frequency. A graphical representation is shown in fig. 2.1.

2.2 Nonlinear Optics

Nonlinear optics is a branch of optics that studies the phenomena that occur when material is exposed to light, usually of a high intensity, that change the optical properties of the material [16, 17]. The term “nonlinear” refers to the fact that the responses of the material is nonlinear in its dependence on the the strength of the applied optical field [16]. A material’s polarisation density $\vec{P}$ refers to the dipole moment per unit volume induced by an applied electric field [18]. From [19], the polarisation density $\vec{P}$ in nonlinear optics is given by the series expansion:

$$P = \chi^{(1)}E + \chi^{(2)}E^2 + \chi^{(3)}E^3 + \chi^{(4)}E^4 + \ldots, \tag{2.2}$$

where $\chi^{(n)}$ is the n-th rank susceptibility tensor of the material. The light-matter energy change per unit time and volume is given by:

$$\frac{dW}{dt} = \left\langle \vec{E} \cdot \dot{\vec{P}} \right\rangle. \tag{2.3}$$

2.2.1 Two-photon absorption

Two-photon absorption (2PA) is a process where an atom or molecule is excited through the simultaneous absorption of two photons. The combined energy of both photons is enough for a transition from the ground state to an excited state to occur, even though the absorption of only one of the photons would not have been enough. In this case eq. (2.1) becomes:

$$E_{\gamma 1} + E_{\gamma 2} = \hbar\omega_1 + \hbar\omega_2 = \Delta E = E_1 - E_0, \tag{2.4}$$

For 2PA to occur, the two photons must arrive within an interval in the order of magnitude of 10^{-16} seconds [20]. If two photons have the same energy, the transition probability for the 2PA process depends on the square of the intensity of the light beam used for the excitation [21]. A comparison between one- and two-photon absorption is shown in fig. 2.1.

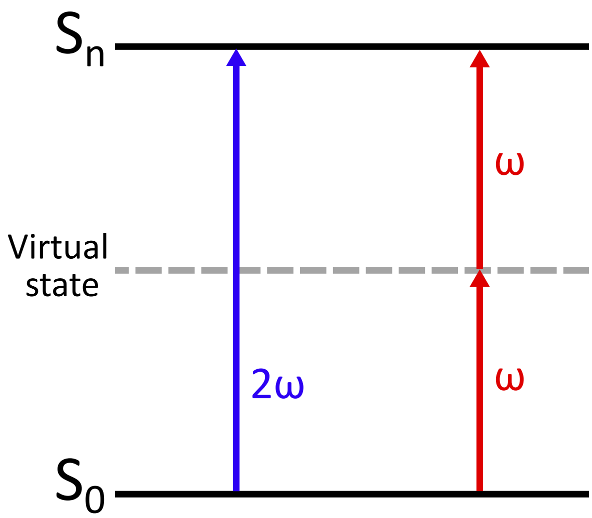

Figure 2.1: A transition scheme showing the transition from the ground stare S_0 to an excited state S_n comparing 1PA and 2PA for a case that $\omega_1 = \omega_2$

In relation to eq. (2.2) and taken from [19], in the case of resonant processes, only the imaginary parts corresponding to odd n contribute. The tensor $\chi^{(3)}$ corresponds to 2PA. For 2PA of two photons of the same frequency, the light-matter energy change per unit time and volume becomes:

$$\frac{dW}{dt} = \frac{8\pi^2\omega}{c^2n^2} I^2 \operatorname{Im}\left\{\chi^{(3)}\right\}. \tag{2.5}$$

The capacity to absorb photons via 2PA is given by the 2PA corss section δ:

$$\frac{dn_p}{dt} = \delta N F^2, \tag{2.6}$$

where N is the number of absorbing molecules n_p is the number of absorbed photons and F is the photon flux defined by $F = I/h\nu$. This is related to eq. (2.5) via the following equation:

$$\delta = \frac{8\pi^2 h\nu^2}{c^2n^2N} I^2 \operatorname{Im}\left\{\chi^{(3)}\right\}. \tag{2.7}$$

2.3 Photopolymers

Photopolymers are a class of materials whose properties change when exposed to light, often in the form of hardening through a process called photopolymerisation [22]. Photopolymerisation occurs when an absorbed photon initiates a chemical reaction that binds monomers and oligomers together through cross-linking. When the chemical reaction is sustained, the binding results in the creation of polymer chains. An example of a monomer used in direct laser writing is pentaerythritol triacrylate (PETA) [23], which is shown in fig. 2.2.

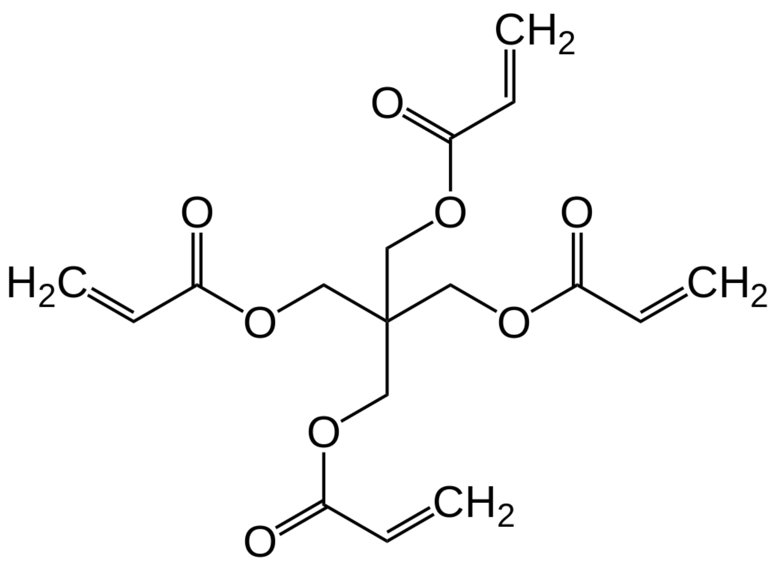

Figure 2.2: An illustration of PETA [23].

2.3.1 Radical Polymerisation

As taken from [24, 25], radical polymerisation in photopolymers is a mechanism that occurs when photoinitiators are irradiated to produce radicals. This is the first step in such a chemical reaction and is known as the initiation of the reaction. The free radicals bind with monomers, the building blocks of polymers, to create a new radical. This starts the growth of a polymer chain as the new radical attaches itself to other monomers. This is the second step of the reaction, known as propagation. The polymerisation continues until two radicals meet and terminate the chain. The reaction can also be terminated if the radicals are disturbed by radical scavengers such as oxygen or other impurities. This is the third step in the reaction, known as termination. A scheme for radical photopolymerisation reaction is shown here [25]:

$$\begin{aligned}
\mathrm{PI} &\xrightarrow{h\nu} 2\mathrm{R}^\bullet \\
\mathrm{R}^\bullet + \mathrm{M} &\longrightarrow \mathrm{RM}_1^\bullet \\
\mathrm{RM}_n^\bullet + \mathrm{M} &\longrightarrow \mathrm{R(M)}_{n+1}^\bullet \\
\mathrm{R(M)}_n^\bullet + \mathrm{R(M)}_m^\bullet &\longrightarrow \text{Inactive polymer.}
\end{aligned}$$

Here, PI is the photoinitiator, $\mathrm{R}^\bullet$ is the initiating radical and M is a monomer.

The reaction can also be terminated by a terminator radical [26] in a controlled radical photopolymerisation reaction. A scheme for this type of polymerisation is as follows [26]:

$$\begin{aligned}
\mathrm{R\text{-}DC} &\xrightarrow{h\nu} \mathrm{R}^\bullet + \mathrm{DC}^\bullet (h\nu) \\
\mathrm{R}^\bullet + \mathrm{M} &\longrightarrow \mathrm{RM}^\bullet \\
\mathrm{RM}_n^\bullet + \mathrm{M} &\longrightarrow \mathrm{R(M)}_{n+1}^\bullet \\
\mathrm{R(M)}_n^\bullet + \mathrm{DC}^\bullet &\leftrightarrows \mathrm{R(M)}_n\text{-}\mathrm{DC}^\bullet (h\nu).
\end{aligned}$$

Here, R-DC acts as a photoinitiator, $\mathrm{R}^\bullet$ is the initiating radical, $\mathrm{DC}^\bullet$ is the termination radical and M is a monomer.

2.4 Optical fibres

Optical fibres are dielectric wave guides comprised of a core with a refractive index n_{core}, through which light traverses, and a cladding that envelops the core with a refractive index n_{cladding}, that operate on the principle of total internal reflection [17]. For this, the condition $n_{\text{core}} > n_{\text{cladding}}$ must be met. Optical fibres are made from low-loss materials such as silica glass [27]. There are two main types of fibres: single- or multi-mode fibres. Single-mode fibres only allow one light mode to propagate and have a core width typically between 2 µm and 9 µm. In contrast, multi-mode fibres have wider cores, typically 50 µm to 800 µm allowing multiple modes to be sent simultaneously [17, 28].

The numerical aperture (NA), acceptance angle θ and the refractive indices n_{core} and n_{cladding} are related as follows[29]:

$$\mathrm{NA} = \sin\theta = \sqrt{n_{\text{core}}^2 - n_{\text{cladding}}^2} \tag{2.8}$$

This describes at what angle light can be shone into the fibre for it to propagate through the core. The cross section of an optical fibre is shown in fig. 2.3.

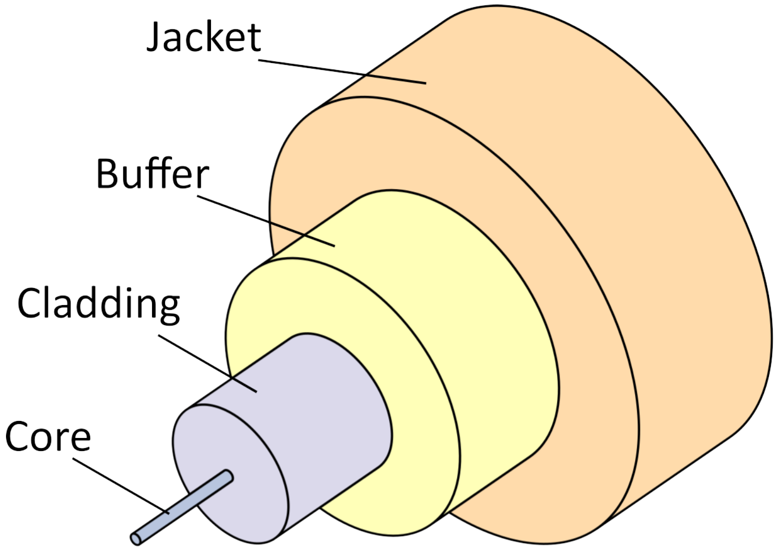

Figure 2.3: An illustration of a cross-section of a single-mode fibre as it is used in a laboratory setting [30].

2.5 Gaussian Beams

A Gaussian beam is a beam of EM radiation whose amplitude envelope in the transverse plane can be described by a Gaussian function [31]. Mathematically, a Gaussian beam is the solution to the parallax wave equation[32, 33]. In practice, the output of most lasers can be described through the fundamental transverse Gaussian mode [31, 32].

The following equation gives the electric field of a Gaussian beam [33]:

$$E(x,z) = A_0 \frac{w_0}{w(z)} \exp\left(-\frac{x^2}{w(z)^2}\right) \exp\left(-ik\frac{x^2}{2R(z)} - ikz + \phi(z)\right) \tag{2.9}$$

where:

- A_0: complex amplitude,
- w_0: beam waist radius,
- $w(z)$: beam radius as a function of z,
- k: wave number,
- $R(z)$: radius of curvature of the wavefront,
- $\phi(z)$: Gouy phase shift.

These parameters are defined for a wavelength λ as follows [33]:

$$w_0 = \sqrt{\frac{\lambda z_R}{\pi}} \tag{2.10}$$

where z_R is the Rayleigh length, defined as the length where $w(z) = \sqrt{2}w_0$,

$$w(z) = w_0\sqrt{1 + \left(\frac{z}{z_R}\right)^2} \tag{2.11}$$

$$R(z) = z\left(1 + \left(\frac{z_R}{z}\right)^2\right) \tag{2.12}$$

$$\phi(z) = \arctan\left(\frac{z}{z_R}\right) \tag{2.13}$$

The divergence of the beam is related to the beam waist radius and the wavelength through [31]:

$$\theta \approx \frac{\lambda}{\pi w_0} \tag{2.14}$$

and the full width at half maximum (FWHM) is related to the beam radius through:

$$w(z) = \frac{\mathrm{FWHM}(z)}{\sqrt{2\ln 2}}. \tag{2.15}$$

The intensity of the beam is given by [33]:

$$I(x,z) = I_0\left(\frac{w_0}{w(z)}\right)\exp\left(-2\frac{x^2}{w(z)^2}\right) \tag{2.16}$$

with

$$I_0 = \frac{2P_0}{\pi w_0^2} \tag{2.17}$$

and P_0 being the Power of the beam.

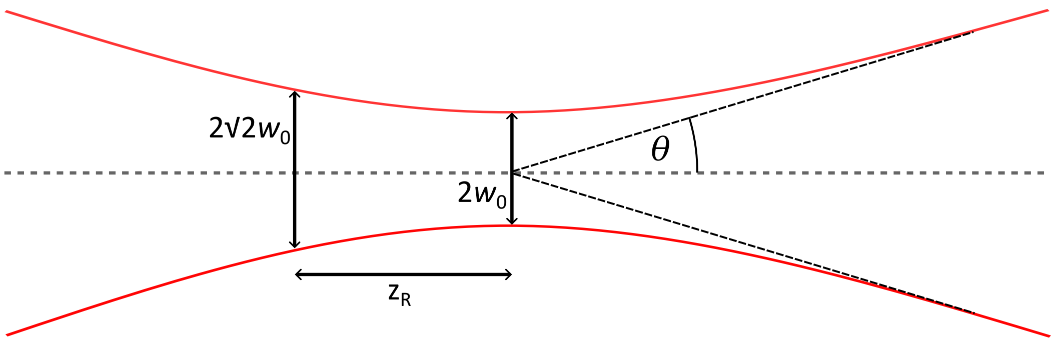

Figure 2.4: An illustration of a Gaussian beam with its parameters.

2.6 Collimating Lenses

In ray optics, a collimated light beam is defined as a beam of light whose rays are parallel. To achieve a collimated beam, one would place a point light source exactly one focal length away from a focusing lens [17, 34]. An ideal point source will lead to an undiverging beam. In a real-world setting, we will always have a non-ideal point source that has a spatial extent, so there will be divergence as some rays will not be completely parallel. The amount of divergence is proportional to the size of the light source and inversely proportional to the focal length of the collimating system [34].

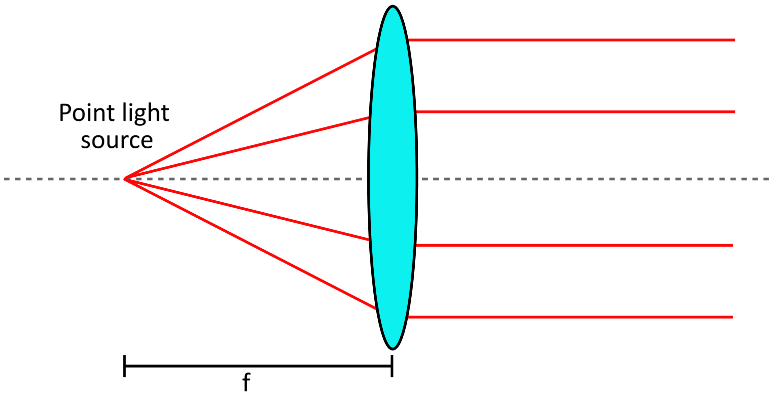

Figure 2.5: An illustration of collimation of light from a point source.

In the context of Gaussian beam optics, a collimated beam has a low beam divergence and a very long Rayleigh length. A theoretical beam with an infinite radius of curvature $R(z = 0) = \infty$ is close to a planar wave [33]. To achieve such a beam from a Gaussian beam with a beam waist radius w_0, one would place the focus of a thin lens f at w_0, resulting in a collimated beam waist[33, 35]:

$$w_{\text{col}} = \frac{\lambda f}{\pi w_0}. \tag{2.18}$$

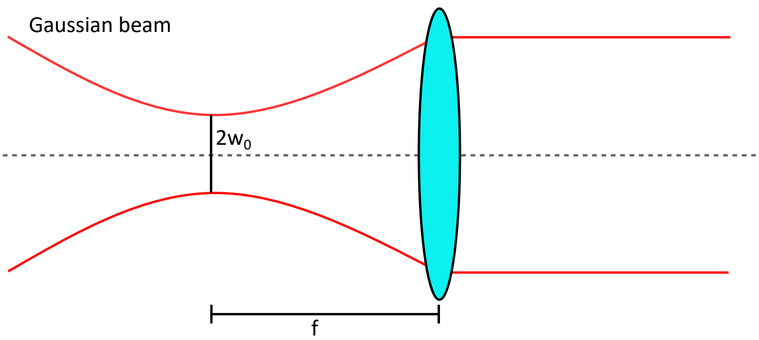

Figure 2.6: An illustration of collimation of a Gaussian beam.

CHAPTER 3

Design and Production Methods

Having outlined the theoretical aspect in the previous chapter, this chapter now introduces the experimental setups and fabrication methods used throughout this thesis. This chapter starts with an introduction to direct laser writing. Following this, the functions and features of the Nanoscribe Photonic Professional GT+ 3D printing system are introduced.

3.1 Fabrication via Direct Laser Writing

Direct laser writing is a fabrication technique that utilises a laser to induce photon polymerisation in a photoresist. By controlling the positioning of the laser, one can polymerise the photoresist in certain areas, creating polymerised structures where the laser beam has passed [36] . This technique can be used for a laser corresponding to the photoresist's polymerisation threshold to create 2D/2.5D structures [37]. It lacks the ability to create 3d structures, as all the molecules in the path of the beam as it passes through the resist will polymerise [38].

To create 3D structures, 2PA is utilised and offers high resolution when using a highly focused laser beam. The laser used should have a wavelength for which the photoresist is transparent but should be at least half the polymerisation threshold of the resist [36]. For this type of direct laser writing, a laser with femtosecond pulses and an objective with a high NA is usually used [39]. Due to the nature of the focused laser beam and the necessary intensity needed for 2PA to occur, only a very small volume of the resist will experience photon polymerisation [36, 39]. This volume, known as a voxel, can be controlled in 3 dimensions. A comparison between 1PA and 2PA is shown in fig. 3.1.

3.2 Nanoscribe Photonic Professional GT+

The Nanoscribe Photonic Professional GT+ (PPGT+) is a commercially available micro- and nanofabrication system sold by Nanoscribe GmbH & Co. KG. The system allows the production of polymer structures through 3D printing via direct laser writing, utilising two-photon polymerisation. The main features of the Photonic Professional GT+ will now be introduced. Unless stated otherwise, the following information is taken from Nanoscribe's online recourse library [41].

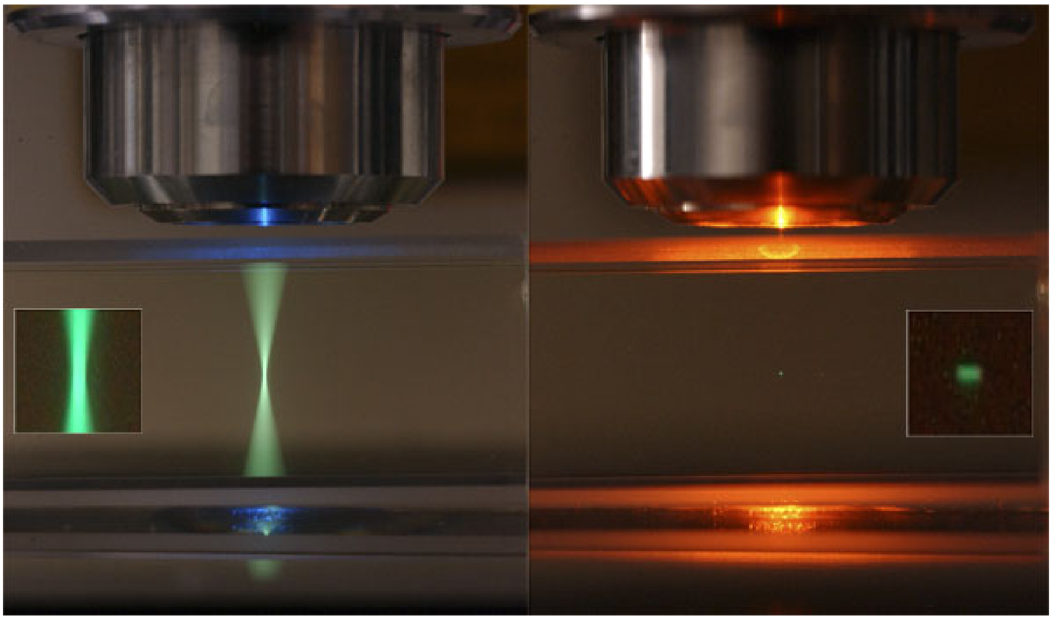

Figure 3.1: A comparison of fluorescence from 1PA(left) at 488 nm and 2PA(right) at an infrared wavelength in a sample of dilute fluorescein solution in a quartz cuvette. The magnified inserts are the beam waist and voxel, respectively. From [40]

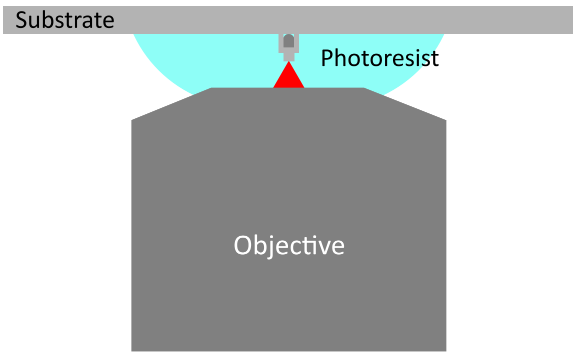

Figure 3.2: On the left an illustration of direct laser writing using dip-in laser lithography. On the right is an photograph of the PPGT+.

3.2.1 Laser

According to the PPGT+ operating manual [42], the system utilises a laser that operates at a 780 nm wavelength and has a pulse duration lying between 80 fs and 120 fs. Coupling the repetition rate of 80 MHz and a peak power of 25 kW results in an average output power of less than 180 mW.

3.2.2 Stages

The PPGT+ has two separate stages used to position the substrate on which the desired structures are printed. The first stage is a mechanical stage used for larger movements of the substrate in the x-y direction, for example, moving from one print location to another. The second stage is a piezo stage which is attached to the mechanical stage. The piezo stage allows precise movement in x-y-z direction in a volume of 300 µm × 300 µm × 300 µm.

3.2.3 Z-drive

The mechanical z-drive is responsible for moving the microscope objective in the z-direction. Its primary purpose is moving the objective towards the substrate in order to find the interface between the photoresist and the substrate. It can also be used when printing objects that go beyond the range of the piezo drive, allowing a maximal print height of 8 mm.

3.2.4 Finding the Interface

For 3D printing to occur on the substrate's surface, the interface between the photoresist and the substrate must be found. The system automatically finds this by using a contrast in the refractive indices of the two materials. This is an important step in the printing process, as the printed structure will float away without proper attachment to the substrate.

3.2.5 Writing Modes

The PPGT+ allows 3D printing via two distinct modes; the galvo printing mode and the piezo printing mode. The galvo mode uses the positioning of two mirrors relative to each other to steer the laser beam across the substrate. The size of the printable field is dependent on the lens used. The galvo mode can be used with either the piezo z-axis positioner or the mechanical z-drive and is best suited for fast printing. The piezo printing mode uses the movement of the piezo stage relative to the stationary laser beam. As there is high spatial control through the piezo stage, this printing mode is best for highly detailed prints, with a trade-off being that this printing mode is up to 100 times slower than the galvo mode.

3.2.6 Microscope Objectives

The PPGT+ can utilise three objectives for 3D printing, each corresponding to different print characteristics. The 63x objective is suited for printing small structures, typically up to a print volume of 0.1 mm^3 in size. The 25x objective is suited to medium-sized prints with a print volume up to 50 mm^3. The 10x objective is used for larger prints with less focus on detail, with a maximum recommended print volume of 400 mm^3. An example of the size of the writing fields for each lens is shown in fig. 3.3.

3.2.7 Photoresists

Nanoscribe also serves as a vendor for photoresists compatible with the printing system. The different types of photoresists are designed for specific uses but are all based on the principles of being a

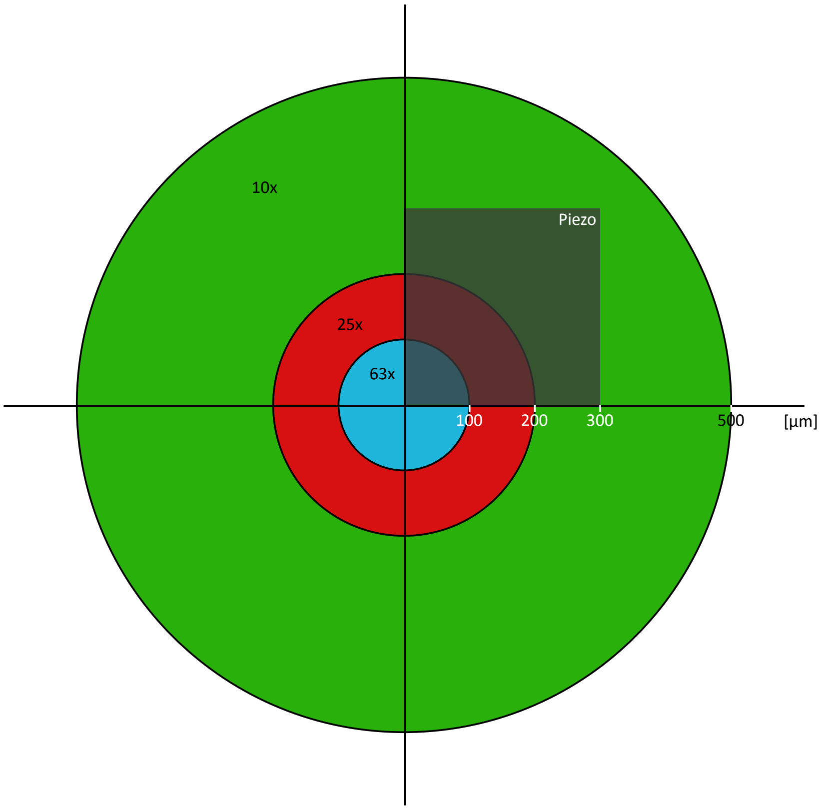

Figure 3.3: A comparison of the size of printing fields of the 63x, 25x and 10x objectives as well as the size of the piezo range.

mixture of monomer/oligomer and a photoinitiator. The manufacturer does not publish the exact composition of the photoresists, but the comparison between the chemical safety sheets of IP-S resist and PETA[43] plus photoinitiator shows both materials containing the same hazardous materials [44].

3.3 Designing and Importing Structures

The design process for 3D printing using the PPGT+ is based on computer-aided design (CAD). The desired structures are designed using CAD software, which can export the designs in the stereo lithographic (STL) file format. The CAD software Fusion 360 (Autodesk, Inc.) was used for this thesis. The software DeScribe (Nanoscribe GmbH & Co. KG.) can read the STL files. This software converts the STL files into a format that the PPGT+ can read and generate print job files. The DeScribe import wizard makes the generation of print jobs easier by eliminating the need to program the print job manually but giving the option of using preset parameters or inputting the desired parameters in a graphic user interface (GUI). The DeScribe software exports files in the general writing language (GWL) format, a file type developed by Nanoscribe. The GWL files contain the commands to read the files containing the trajectories along which the lase moves during printing. The trajectories are saved in either GWL or GWLB files. The difference is that the GWL file can be manually edited by opening it in either DeScribe or Windows Notepad, whereas the GWLB file is only machine-readable.

3.4 Printing Parameters

The following section outlines the most important parameters used when printing using the PPGT+.

3.4.1 Slicing and Hatching Distances

The slicing distance refers to the distance between the individual layers of the printed structure. The voxel is moved in the z-direction between the printing of each layer; this movement corresponds to the slicing distance. The slicing distance is usually selected to be smaller than the voxel height so that there is an overlap between layers. A smaller slicing distance will result in a finer print but a longer print time.

The hatching distance corresponds to the distance the voxel is moved in the x-y-direction between laser pulses. As with the slicing distance, the hatching distance is selected so that there is sufficient overlap of the voxels with each laser pulse. Decreasing the hatching distance will also increase the quality of the print but also the printing time. A visualisation of slicing and hatching distances is shown in fig. 3.4.

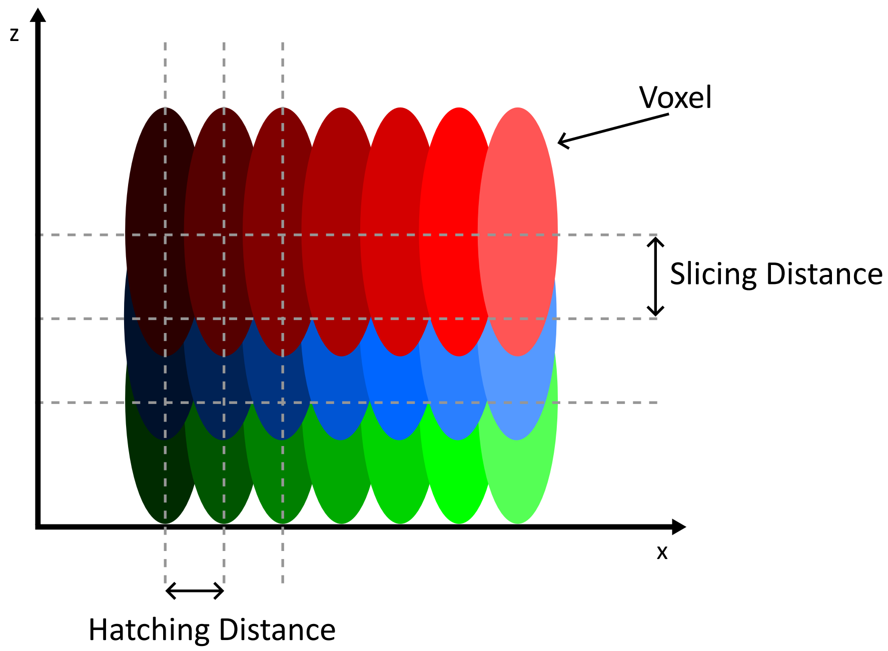

Figure 3.4: A visualisation of the slicing and hatching distances in two dimensions. The different colours and shades are used only to contrast voxel positions.

3.4.2 Scan Speed and Laser Power

Scan speed and laser power are two parameters that complement each other in the printing process. During the writing process, the scan speed controls the speed at which the voxel is moved across the printing field. The laser power parameter is a percentage of the total laser power. When deciding the values for printing, a balance must be found as both parameters affect the dose the resist receives.

Selecting the wrong values will result in either a dose too low for polymerisation to occur or a dose too high, resulting in overexposure and the destruction of the printed structures. Therefore, it is recommended to perform a parameter sweep to find suitable parameters for printing, as seen in fig. 3.5. In the sweep shown, the effect of a laser dose that is too low can be seen. A parameter sweep should be performed when a new supply of resist is used, as slight differences in production or ageing of the resit can result in the ideal laser dose changing.

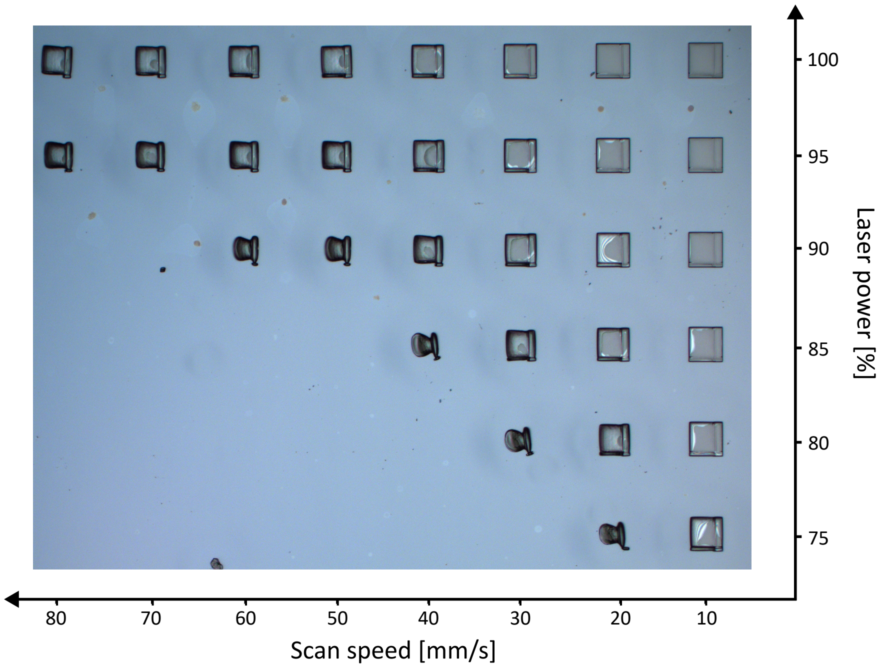

Figure 3.5: An example of a parameter sweep testing different combinations of scan speed and laser power for IP-S photoresist and 63x objective. or scale, each block has a width of 120 µm.

3.4.3 Shell, Scaffold and Solid Printing Functions

When creating a job file using the DeScribe import wizard, the software gives the choice of printing function: shell, scaffold or solid. This shell printing function prints only the outer shell of the structure. Within this shell remains unpolymerised resist. The scaffold printing function adds an internal structure scaffold to the shell, giving more structural stability but still leaving unpolymerised resist. The solid printing function prints a completely solid structure, leaving behind no unpolymerised resist. In the case of shell and scaffold functions, the structure must be cured with UV light to polymerise the resist within the shell. The type of printing function should be chosen depending on the requirements of the printed structure. Solid printing mode should be used for high precision and structural stability, whereas shell and scaffold should be used to decrease print time if the internal structure of the print is not of importance.

3.4.4 Block Splitting

Block splitting is a feature of the DeScribe software that allows printing structures larger than the writing field. The imported structure is split up into smaller sections that fit into the writing field. DeScribe generates a print job file that controls stage movement and the importing of the blocks. In the import wizard, the order in which the blocks should be printed, the shear angle between the blocks, and block overlap can all be specified if needed.

3.5 3D Printing with the PPGT+

The following section outlines the dip-in printing process recommended by Nanoscribe through their online resources [41]. This process must be adjusted depending on the size of the desired structure but the overall process remains the same. First, a substrate is cleaned with isopropanol (IPA) and blow-dried with nitrogen. The substrate is then attached to the sample holder using insulating tape. For dielectric-coated substrates, the coated side must face upwards, allowing the interface to be found. The photoresist is then applied to the substrate. The desired objective is then screwed into its corresponding position in the objective holder. The Nanowrite software (Nanoscribe GmbH & Co. KG.) is then started, and the mechanical stage is calibrated. Following this, the sample holder is inserted, and the objective is driven upwards in order to perform an interface find between the resist and the substrate. The print job GWL file is then loaded, and the print job is started.

3.5.1 Development Process

After printing has been completed, the substrate is removed from the printer. The print job must then be developed in order to wash away the unpolymerised photoresist. This is done using propylene glycol methyl ether acetate (PGMEA) in order to dissolve the liquid resist. The time needed for all resist to be dissolved varies from print to print but a minimum development time of 20 minutes in PGMEA is recommended. The print is then soaked in IPA for around 10 minutes in order to wash away the developer, but shorter soaking times can be used in order to avoid slight deformation or swelling of the polymer that can occur when it is in contact with IPA. It is important that the development takes place in an environment without possible UV-light contamination to avoid unwanted polymerisation of excess resist.

CHAPTER 4

3D Printing of Lenses for Fibres

This chapter outlines the design and printing of collimating lenses used on the end of optical fibres. First, the challenges of fibre-end printing are presented, followed by the introduction of a design of a new optical element for printing the collimating lenses on a substrate. The rest of the chapter focuses on the design details and outlines the printing methods used in its production.

4.1 Background

The printing of collimation lenses onto the ends of single-mode fibres was shown by T. Gissibl et al. in [14, 45]. This work presented a technique that allows the cleaved end of an optical fibre to be printed on using the Photonic Professional GT (Nanoscribe GmbH & Co. KG), which is the direct predecessor to the PPGT+. An attempt to reproduce these lenses was made by us, using a technique for printing on the ends of optical fibres developed by A. Faßbender during his PhD thesis [44]. This technique involved installing a custom-designed substrate holder into the PPGT+ attached to a fibre holder. The fibre tip was then found using the microscope controls and was brought into focus. A manual interface search was then performed by running a program that showed the origin of the x-y printing plane, aligning it with the fibre core and then using the z-drive to find an appropriate z-position for printing.

4.1.1 Difficulties in Manual on Fibre Printing

When using this technique to print directly onto the fibre, difficulties arose in aligning the printed structure with the fibre core. An example of this can be seen in fig. 4.3. Furthermore, performing the manual interface find also proved challenging. Staring the print with the interface too far inside the fibre would result in the desired structure being shorter than required, and staring the print at or above the fibre end would result in inadequate adhesion of the print. A further difficulty of this printing technique is the long time it takes for such a print to be made. Part of the illumination setup must be removed for the fibre holder to fit into the printing setup, adding time to preparing the pint job. Locating the fibre using the stage controls and finding the print interface manually is time-consuming and must be performed for each fibre. This printing configuration can also only accommodate one fibre. Due to this, this thesis investigates a new technique for more accurate alignment and faster repetition of the prints.

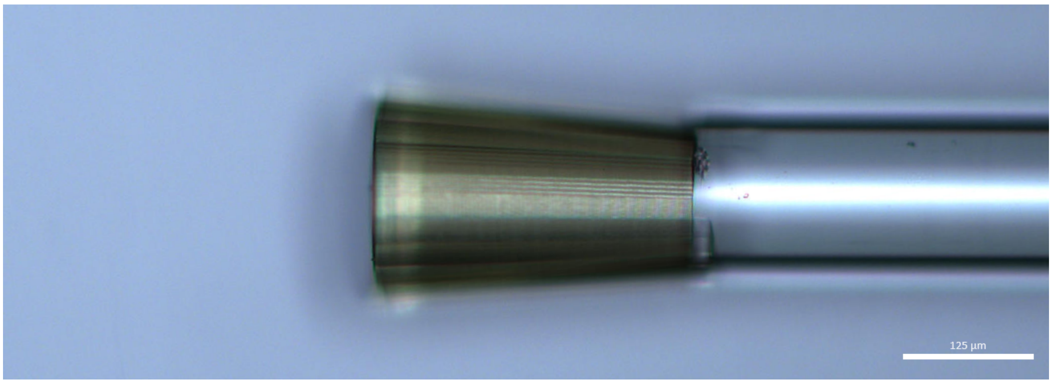

Figure 4.1: The lens base of the 300 µm lens from [14] printed on the end of a single mode fibre. Imaged under a 20x microscope objective. Note the misalignment of the lens base to the fibre end.

4.1.2 Fibres in 3D Printed Masks

A. Faßbender developed a technique for 3D printing polymeric masks for use on optical fibres in [44]. In this work, metallic structures were created on fibres using the shadow of the masks during evaporation. In order to create complex metal structures on the fibres, two masks had to be used in secession, and the geometry of the masks allowed the evaporated structures to be aligned. Using a similarly designed mask was a potential solution for the difficulties in aligning the optical fibres with a lens. Such a mask allows the fibre to move in only one direction by guiding the fibre in a similar fashion to a ferrule, allowing the fibre core to be positioned precisely. The inaccuracies in alignment should be greatly reduced by printing the lens attached to a polymeric lens at a position exactly over the core.

4.2 Outline of Lens Design

The lens design is based on the printing methods used by T. Gissibl et al. in [14, 45]. The goal was to find a printing technique that would allow the printing of multiple lenses simultaneously, which is achieved by moving away from fibre-end printing and printing an array of lenses onto a substrate. A second goal was to implement a mask as described in subsec. 4.1.2 into the design, with the aim of using friction and der Waals forces to attach the mask to the fibre.

A further goal was to keep the same printing parameters as used by Gissibl et al. In designing the lenses, the 250 µm lens thicknesses (D) collimating lens with a radius of curvature (ROC) of −85.8 µm by Gissibl et al. is used as a base reference. Replicating the slicing and hatching distances used by Gissibl et al. for their free-form beam shapers, as detailed in [14, 45], ensures consistency in print parameters, allowing direct comparison and evaluation of the new approach. When printing the lenses oriented vertically to the substrate, the lens's orientation on the end of the fibre is replicated. This approach to printing minimises external variables, ensuring that any errors can be attributed to the flaws in the design rather than to the lenses themselves. On the other hand, the goal was to keep the design simple enough to be adapted to other types of lenses.

4.3 Final Design of the Optical Element

Figure 4.2: A render of the optical element as it is printed on a glass substrate.

In fig. 4.3, a CAD render of the final design of the optical element (OE) is shown. The design can be divided into three main parts, each serving a distinct function. The first part of the design is the lens. The lens used throughout the lens development corresponds to the same dimensions as the 250 µm collimating lens produced by Gissibl et al. However, the optical element was not designed around this particular lens; instead, it was designed so that the lens could be easily exchanged for a lens of other dimensions. This is further discussed in section sec. 4.8. The second part of the optical element is the stand to which the lens is attached. The stand allows the lens to be printed vertically and acts as the primary connection point between the substrate and the optical element. The third part is the mask, which is printed on top of the stand. The mask is designed to be a few micrometres wider than the fibre width to allow efficient insertion and provide enough surface contact for the OE to attach itself to the fibre.

4.4 Design Overview of the Optical Element

This section discusses the individual parts of the optical element's design. This overview aims to give insight into the design philosophy and explain the logic behind the design choices made.

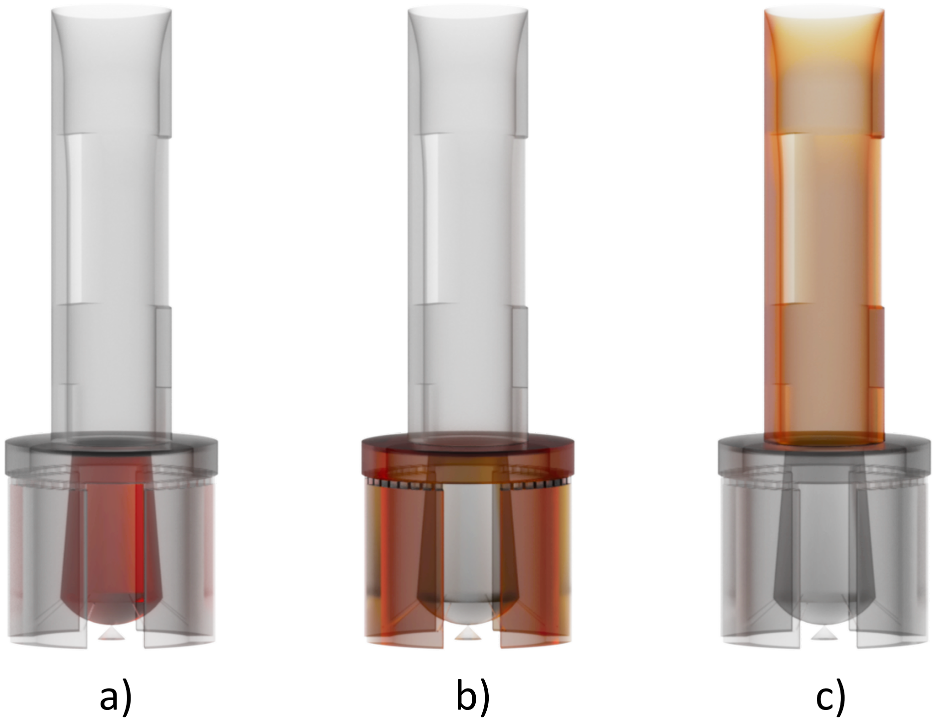

Figure 4.3: A render highlighting the different parts of the OE in colour. a) lens, b) stand, c) mask

4.4.1 Dimensions of Design

The size of the OE was chosen so that it could be printed with the 63x objective, the same objective used in [45]. The print field of diameter 200 µm associated with this objective was found not to be a hard limit on the size of structures that could be printed. A test was performed where circles of increasing diameter were printed, and it was found that 300 µm was the maximum diameter that the structure could have. As such, 300 µm was selected as the diameter of the outermost parts of the stand in order for the spacing between the lens and the stand to be maximised.

The maximum thickness of the lens that can be printed is limited by the piezo range and the support structures needed for printing. The piezo printing mode is used for printing and has a maximum range of 300 µm in z-direction. Usually, structures exceeding this size are split, and the z-drive re-positions the sample. This is not an option when printing the lens, as the z-drive's movement could disturb the lens as it is printed, as it only has minimal support during printing. Along with the maximum height of 300 µm the combination of lens and stand can have, the support structures of the lens have a height of 20 µm, resulting in a maximum distance of 280 µm form the tip the of the lens to top the of the stand.

4.4.2 Support Structures

In order for the lens to be printed vertically with the curved refractive surface facing the substrate, support structures are needed for this design to be realised. Printing a hanging lens proved challenging due to the difficulties of printing a free-floating structure. In galvo printing mode, there is no stage movement during printing, and basic free-floating structures can be printed. The challenges in printing a lens are the high precision in alignment and the need for homogeneity in the internal structure. It was found that even the slightest disturbance of the lens through movement would result in a lens that could not refract light as intended. It's suspected that the photoresist flows very slightly during printing, which could explain the disturbance. Another possible source could be the thermal changes throughout the printing process. Attempts were made to address these possible disturbances but were ultimately unsuccessful. More on this can be found in subsec. 4.5.5.

Two support structures fixate and stabilise the lens from the bottom and the side. The bottom support structure is needed to hold the refractive part of the lens in place while it is being printed. The support is in the shape of a cone in order to maximise surface contact with the substrate and minimise the contact point between the support and the lens. Due to the size of the voxel and the printing parameters used, the support structure can be designed to be slightly smaller than the gap between the tip of the lens and the substrate. It was found that a gap of 2 µm in the CAD design between the tip of the cone was the lower limit for consistent connection to occur. The cone height of 18 µm is combined with a base diameter of 20 µm to balance the size of the connection point through the half-angle and the adhesion to the substrate.

The second support structure comes in the form of small arms with the width of 2 µm that connect the side of the lens with the stand. The legs connect to the lens at the transition point from the refractive part to the lens base. The arms are printed along with the refractive part so that they are fully connected to the lens when the refractive part is finished. The primary purpose of the arms is to keep the lens steady as the larger lens base is printed, something that the bottom support structure would not be able to do alone. The choice to use eight arms was made as each foot of the stand is now connected to the lens with two arms, adding stability to the structure.

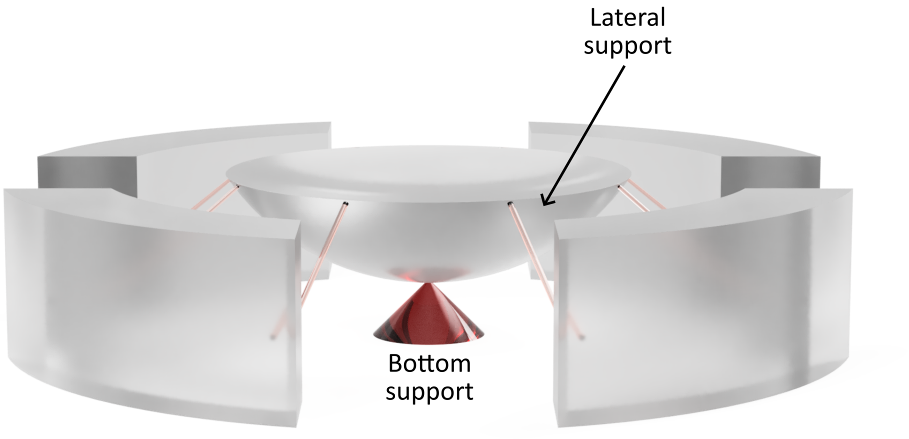

Figure 4.4: A render showing the support structures coloured in red.

4.4.3 Stand

The primary function of the stand is to allow the lens to be printed vertically by connecting to it and holding it in place after printing. The design resembles a round table-like structure with four legs. As the feet of the legs serve as the contact point between the OE and the substrate, the feet' surface area must be large enough for adequate adhesion. On the other hand, the legs have to be as far away from the lens as possible to avoid proximity effects [46]. An internal diameter of 260 µm provided a good balance. The ideal design to maximise the contact surface would be a solid ring, but this can not be implemented as such a structure would not allow the excess resist to be washed away during development. Four 80 µm wide slots are included to allow access to the resist.

The stand is printed at the same time as the lens and holds the lens in place during the printing of the support structures. The lens is connected to the stand through a base plate printed over the top of the legs and the base of the lens and has a thickness of 10 µm. The base plate also acts as the first 10 µm of the base, as the OE is designed to flush the bottom of the lens with the top of the base plate. This is done to keep the distance between the fibre and the end of the lens the same as when printing directly onto the fibre. As the lens and base plate are printed with the same print parameters, this does not affect the beam's dispersion through the base. At the connection between the legs and the base plate, a weak spot is included in the form of a small 13.6 µm × 10 µm holes evenly spaced 5.2 µm apart. These holes allow the legs to be mechanically removed from the OE if desired. The inclusion of such a weak spot was not observed to cause a decrease in the structural stability of the OE. A render of the stand can be seen in fig. 4.5.

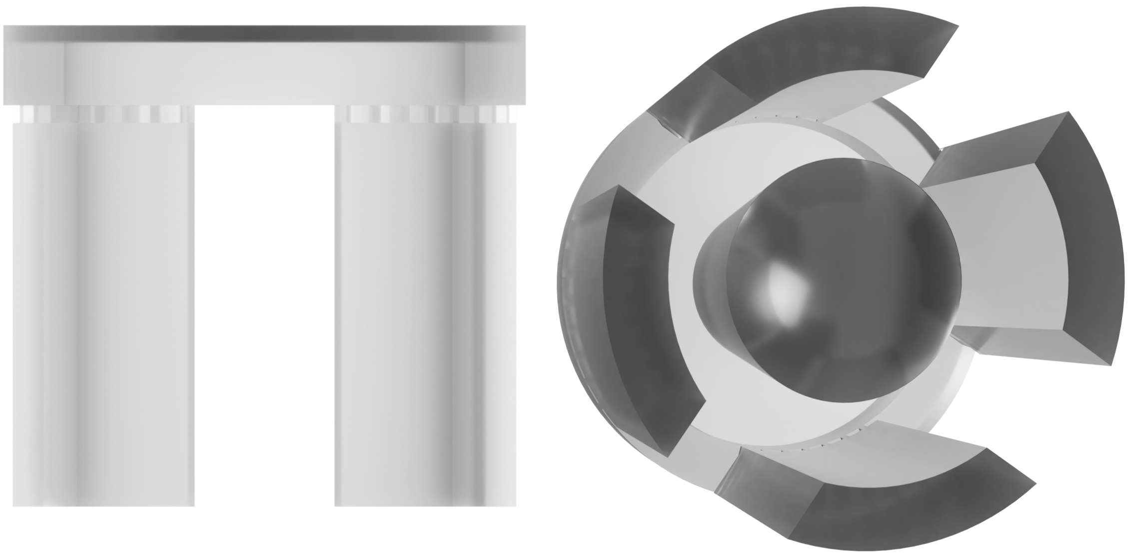

Figure 4.5: On the left: a render showing the stand from the side. On the right: A render showing the connection between the lens and the stand without support structures included.

4.4.4 Mask

The mask design is based on the masks developed by Alexander Faßbender in [44]. The mask has a length of 608 µm and an external width of 170 µm. The length was chosen, as along with positioning and guiding the fibre to the lens, the mask must also act as the connection point between the fibre and the OE. The OE is attached to the fibre through friction between the two. In this case, a long mask will result in more surface contact and grip. On the other hand, as the ratio between mask length and width increases, the structural stability decreases. Structural problems such as bending must be avoided as the fibre must pass through the entire mask without being blocked. The mask is printed with drains in the form of slots halfway up the side of the mask and at the connection to the base plate. These allow faster removal of the photoresist from the inside of the mask during development.

The following dimensions are given for a mask designed for a fibre with a cladding diameter of 125 µm. The mask's opening is tapered to guide the fibre into the mask. The internal diameter of 135 µm is then slowly decreased to the desired minimum diameter via a tapered edge. This internal diameter between 1 to 2 µm wider than the cladding diameter of the fibre, was found to allow easy insertion but also sufficient grip to allow the OE to be removed from the substrate.

Figure 4.6: A render showing the mask from the side.

4.5 Printing of Optical Element

This section outlines the printing methods used when printing the optical elements.

4.5.1 Photoresist

In [14], Gissible et al. used the OrmoComp (micro resist technology GmbH) photoresist for printing collimating lenses using the piezo scan mode. Initial attempts to recreate these lenses using OrmoComp on a substrate printed in galvo scan mode were successful. Difficulties arose when trying to print larger structures that involved block splitting, and it became clear that the characteristics of printing with OrmoComp would need to be investigated further. As the design was still in development and an optimal solution had not been found yet (see sec. 4.6), the decision was made to switch to IP-S (Nanoscribe GmbH Co. KG) as it was already known how this photoresist behaves under block splitting. Nanoscribe recommends the IP-S photoresist for the production of microoptics [47] and was used by T. Gissibl et al. for the production of beam shapers using the galvo scan mode, serving as a reference for selecting the printing parameters.

4.5.2 Substrate

The OE is printed on a 25 mm × 25 mm × 0.7 mm indium-tin oxide (ITO) coated substrate. This is the standard for printing with the IP-S photoresist and can be purchased directly from Nanoscribe.

4.5.3 Printing Parameters

The OE is split up into different sections with distinct printing parameters when printing. The first section contains everything from the substrate up to the transition from the refractive surface to the lens base. Here a slicing distance of 0.1 µm and a hatching distance of 0.2 µm is used to achieve fine details on the curvature of the refractive surface. For this section, the hatching angle is set to constant. The second section includes the lens base, stand and base plate. Here a slicing distance of 0.4 µm and a hatching distance of 0.2 µm is used to speed up the printing process. For this section, an automatic hatching angle is used. The final part consists of the mask. When printing the mask, there is no need for a high level of detail, so a slicing distance of 0.7 µm and hatching distance of 0.5 µm is used. The printing parameters are summarised in table 4.1.

Section	Hatching Distance	Slicing Distance	Hatching Angle
Bottom	0.1 µm	0.2 µm	0°
Middle	0.4 µm	0.2 µm	auto
Top	0.7 µm	0.5 µm	auto

Table 4.1: Summary of printing parameters of OE

After performing a parameter sweep over the two parameters, suitable laser power and scanning speed were found. The combination of speed and power that gave a good quality print but minimised overall printing time was a laser power of 100% and a scanning speed of 15 000 µm s^{-1}. These values stayed constant throughout the use of a tube of photoresist. When switching to a different tube, it was found that a new parameter sweep had to be conducted as there was a noticeable change in quality when printing with the print parameters of the old tube.

4.5.4 Importing CAD Files and Programming Print Job

The CAD files of the different sections of the OE are imported individually using the DeScribe import wizard. This is done as it is impossible to set a spatial variation in the printing parameters, making it impossible to set the desired slicing distances for the bottom and middle section of the stand + lens CAD file. The bottom, middle and top sections each have their own printing files that must be combined into a single job file. An example of this is printing the bottom part of a structure on the substrate, adding a z-offset corresponding to the height of the printed structure and then printing the top on the same x-y-coordinates, resulting in a singular structure being printed. This method is the basis for the block splitting method of printing larger structures.

It was found that this method was unsuitable for printing the middle section on top of the bottom section, with problems arising in the form of the two parts not connecting properly or being slightly offset from one another. It is suspected that this is due to the small stop in printing when switching from one file to the other. The problems persisted regardless of whether an interface find was performed before printing the middle section. A solution was found by manually editing the GWL files containing the laser trajectories. For this to be possible, the option “Use NanoWrite 1.7 compatibility mode” must be selected in the DeScribe options. The bottom section is processed using the import wizard with the desired parameters, and a combined CAD model of the bottom and middle sections is processed with the desired print parameters of the middle section. The GWL file of the combined model is now edited by deleting all writing instructions corresponding to the lower section and replacing them with the writing instructions from the GWL file of the bottom section with the required printing parameters. When the print job file of the combination is now executed, the lower and middle sections will be printed with the correct printing parameters.

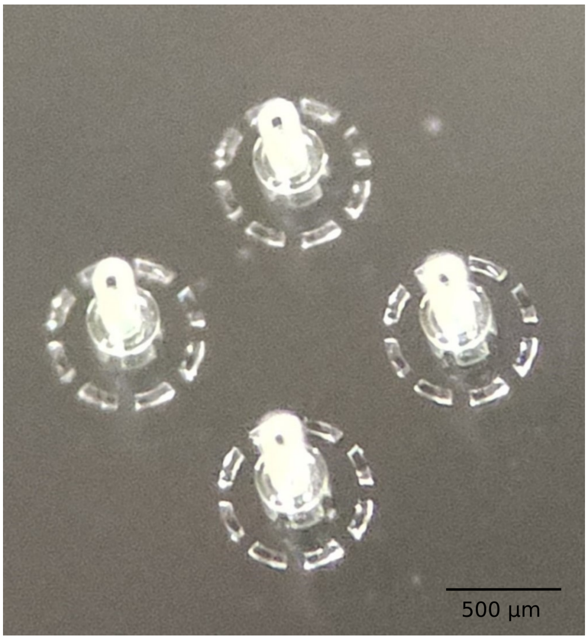

Figure 4.7: An image taken from the 3D preview of an array of four OE being printed. Split up of print job shown. Image taken from DeScribe.

When printing an array of OEs, the 360 µm working distance (WD) of the 63x objective [48] must be taken into account when programming a print job. It is advantageous to print a marker next to the array to distinguish the OEs after printing. The overall height of the OE is much larger than the WD, so printing one OE after the other is not possible. This problem is avoided by printing the first two sections of all OE in the array. As the mask is also taller than the working distance, it must also be split up into manageable sections, which are then printed in a similar manner. When printing the mask, the GWL editing method does not have to be used as fine printing details are not as crucial for the mask and the technique of overlapping the different sections is used for better fixation.

4.5.5 Stabilising Print

A protective structure is preemptively printed around the OE to guard the lens from photoresist flow. This structure resembles a segmented wall, designed with a height of 60 µm to shield the printing of the refractive surface. The primary purpose of this structure is to impede the flow of the entire photoresist pool while still allowing movement of the resist towards the centre as the z-height of the objective increases. After the protective structure is finished printing, the stage is positioned for OE printing and remains stationary for 15 min to ensure equilibrium and minimise unnecessary photoresist flow. Despite these efforts to stabilise the print, disturbances to the free-floating lenses persisted. On the other hand, the protective structure reduced the number of misprints during the development of the lens supports.

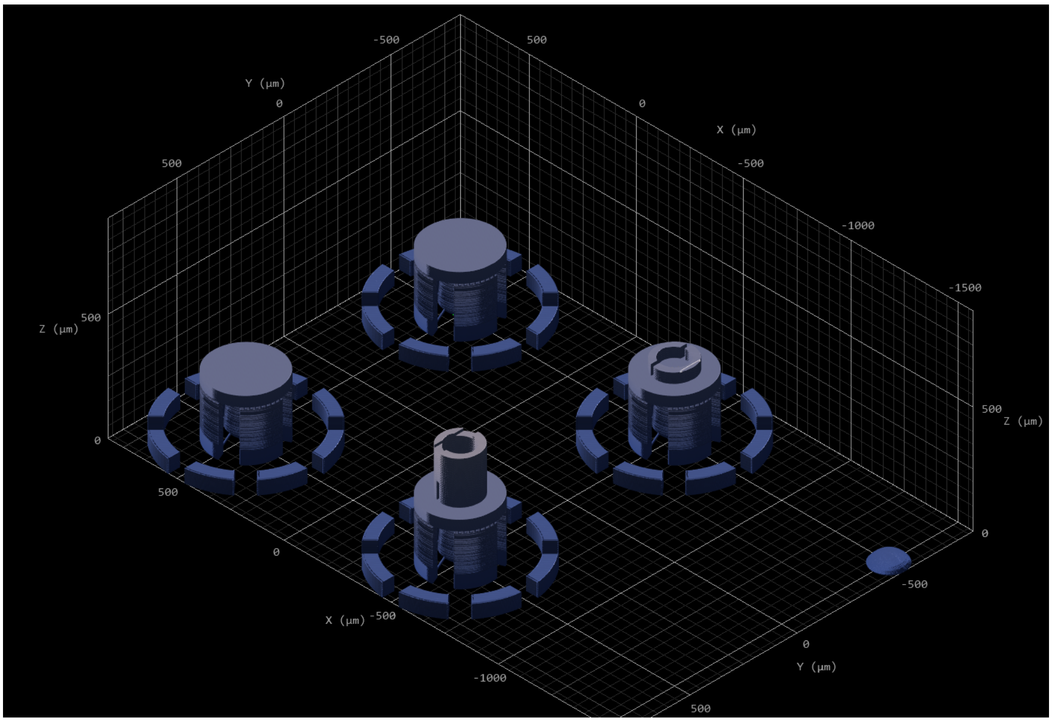

Figure 4.8: An image taken from the 3D preview of an array of four OE being printed. Split up of print job shown. Image taken from DeScribe.

4.6 Progression of Design

This section outlines the different iterations the OE went through in its design.

4.6.1 First Iteration

An initial render of the design is depicted in fig. 4.9. Initially, the four legs of the OE were printed. Subsequently, the lens was initially to be printed in a floating state. Following this, the bridge connecting the lens to the legs was to be printed, followed by the mask.

However, a major challenge encountered with this design was its dimensions. Due to the need for block splitting to accommodate its size, issues arose with the proper connection of smaller sections, leading to frequent structural misalignment. An example of this can be seen in fig. A.1. Additionally, the movement of the stage between sections was found to disrupt the stability of the lens. Another significant issue was the printing of lateral supports for the lens. Initially, without any support, the lens was prone to severe misalignment and would sometimes be dragged along with the movement of the stage. As the legs were printed before the lens, the support structure would need to be printed before the lens. This leads to undesired deformation due to proximity effects seen in fig. A.2.

Due to these difficulties, a functional lens integrated with the rest of the structure could not be achieved, regardless of whether the IP-S or OrmoComp photoresist was used.

Figure 4.9: A render showing the first iteration of the optical element.

4.6.2 Second Iteration

The second iteration, shown in fig. 4.10, is a more compact evolution of the first design and was printed using IP-S. This design also involved printing the feet before the lens. The lens would be attached to the legs by printing a base plate directly on the feet. By making the design more compact, it was hoped that the lens could be printed free floating as block splitting would not be required to attach the lens to the legs, allowing it to float freely while printing.

Problems with this design included the structural stability of the legs. During test prints, the legs would sometimes be crooked or otherwise out of shape, and a reliable solution could not be found for this problem. A further problem was also the stability of the lens. Attempts to print support structures at the same time as printing the lens proved unsuccessful due to difficulties in attaching the structures to the pre-printed legs, and printing both together was not possible due to the total diameter of the structure being greater than 300 µm.

Figure 4.10: A render showing the second iteration of the optical element.

4.7 Attaching Optical Element to Optical Fibre

This section covers the setup and method of attaching the fibre to the end of the optical fibre by inserting it into the mask.

4.7.1 Setup

The setup used for inserting the fibre into the mask is shown in fig. 4.11. The setup is comprised of a microscope (Stemi 305, Carl Zeiss AG, 2× lens), a camp for holding the substrate upright (LFFM1, Thorlabs Inc.) and two micrometer-stages (PT3/M, Thorlabs Inc.). A fibre holder (MDE724, Elliot Scientific Limited) is attached to the right micrometre stage. Attached to the left stage is a cannula that serves as a micromanipulator. This setup is an evolution of a fibre inserting setup used by A. Faßbender in [44].

4.7.2 Technique for inserting fibre

Before the fibre can be inserted into the mask, it must first be prepared to optimise its optical performance. In the case of this thesis, the fibres used were the single-mode 780-HP and the multi-mode FG105UCA (both Thorlabs, Inc.). First, the protective coating is stripped from the fibre. Following this, the fibre is cleaned using a tissue soaked with IPA, and in the final step, the end of the fibre is cleaved.

The fibre is attached to the micrometre stage using the fibre holder. By eye, the fibre can be brought within a few millimetres and roughly onto the same height as the desired optical element. Under the microscope, the tip of the fibre is then brought close to the opening of the mask but not inserted yet. The micromanipulator is used to apply a lateral force onto the OE and push it a short distance to

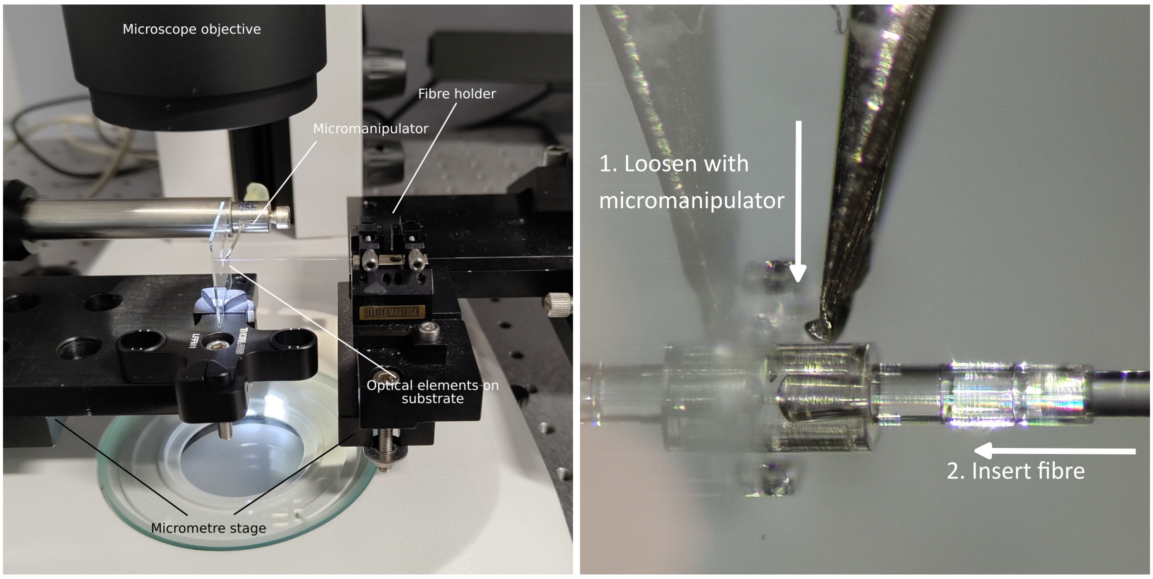

Figure 4.11: Left: Photograph of the setup used for inserting the fibre. Right: Close-up view of fibre being inserted.

loosen the OE from the substrate. The fibre is then slowly inserted fully into the mask, and the OE is lifted from the substrate.

The reason for loosening the OE before the fibre is inserted is due to the connection point between the lens and the bottom support structure. It was found that breaking the connection results in artefacts remaining on the lens at the break-off point (see sec. 5.3). It was found that the size of the break-off point is minimised by breaking the connection before inserting. This is believed to be due to the fibre pushing the lens slightly down and into the support structure when it is being inserted.

4.8 Adapting Optical Element for different lenses

The OE was initially designed with a 250 µm lens used as the benchmark. Despite consistently using this lens during its development, the OE's design isn't exclusively tied to it. Variations are possible, allowing for other lens types to be integrated instead of the 250 µm lens. fig. 4.12 shows the adaptation of the OE design to accommodate a lens length of 136 µm, ROC of −38.1 µm collimating lens, the same ROC as from the 150 µm collimating lens from [14]. The stand has been adjusted to match the reduced length, yet the fundamental structure remains unchanged. The 136 µm lenses are printed using identical parameters and techniques employed for the 250 µm lens. This shows that the OE design isn't limited to a singular lens type but functions as a versatile structure that can be adjusted to accommodate various lens configurations. A further lens that was tested on the OE design was a collimating lens for the use on multi-mode fibres with length 225 µm and ROC 114 µm.

Figure 4.12: A render showing the design of the OE adapted to accommodate a 136 µm lens and 225 µm lens.

CHAPTER 5

Experimental Methods and Results

This chapter outlines the experimental findings from the thesis. The chapter starts with the initial observations of the tip of the lens using conventional light microscopes. Following this, more precise measurements of the lens surface are presented in the form of interferometric data. Finally, the optical performance of the lenses is measured by performing measurements of a propagating beam emerging from the lenses.

5.1 Lens Quality Control

Once the optical element (OE) has finished printing and has been fully developed, the final step undertaken in the production process is to check the quality of the print. Initial checks for significant failures, such as structural collapse, can be done with the naked eye. Following this, a microscope is used to check the finer details of the OE. The quality of the mask and stand can be checked by viewing from the top. The lens can be inspected by viewing through the substrate, for example, by placing the substrate upside down in a sample holder (see fig. 5.1).

Both light- and dark-field microscopy are used to inspect the OE. Light-field microscopy allows the surface of the OE to be examined, which is particularly important for the refractive part of the lens, as defects on the surface can indicate a bad-quality print. Checking the inside of the mask for defects is also advised, as this can indicate if attachment to the optical fibre is feasible. It was found that dark-field microscopy can be used to check the optical quality of a printed lens, making any defects in the lens visible. It was observed that the dark field illumination source, a ring created by the dark field patch stop, was refracted by the lens and could be imaged using an appropriate focus plane. The sharpness of the ring is an indirect indicator of the lens' optical quality. This is shown in fig. 5.2.

5.2 Break-off Point Observation

During the OE's development process, the introduction of the lower support structure brought to light the challenge of the break-off point. From the beginning of prototyping the lower support, it became clear that achieving a clean break-off from this structure would not be possible. As a result, the first step following the optimisation of the lower support structure was to observe the break-off point (BOP) under the microscope.

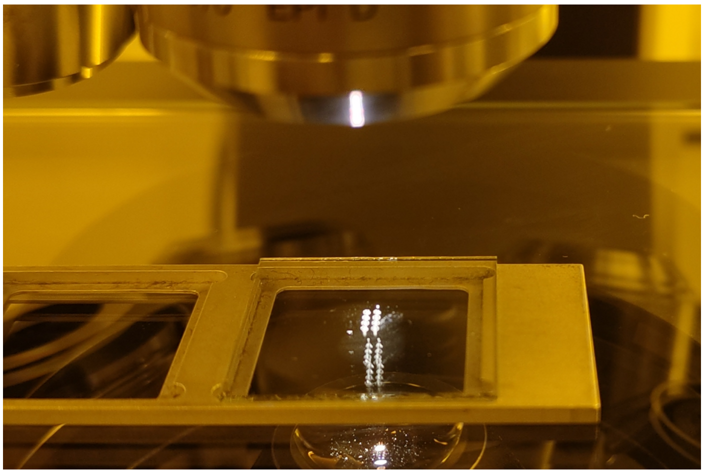

Figure 5.1: The technique used for inspecting the surface of the lenses by observing through the substrate. The holder for a 20 mm slide gives 2 mm of ground clearance, preventing the OEs from coming into contact with the microscope stage.

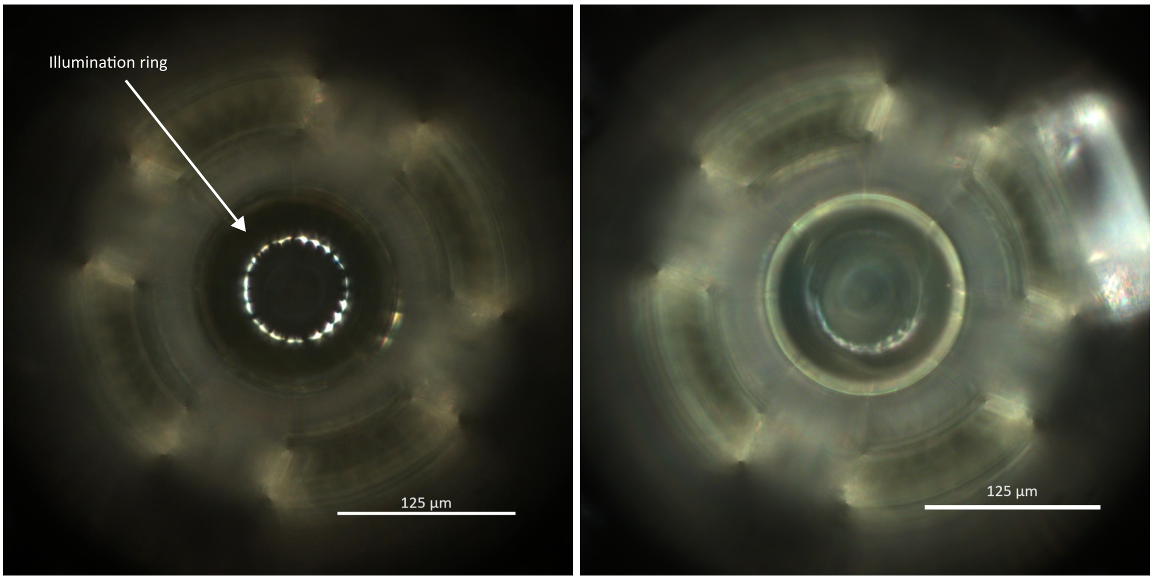

Figure 5.2: A comparison between a lens without defects (left) and a lens with defects (right) where the illumination ring is not imaged properly. Imaged using 20x microscope objective in dark-field mode.

An inverted microscope (DIM5000 M, Leica Microsystems GmbH) was utilised to examine the lens tip. The fibre was positioned within a holder, initially designed for use in the PPGT+ setup for end-of-fibre printing. Optimal observation was achieved by extending the fibre approximately 5 mm beyond the holder's base, ensuring the fibre tip remained within the working distance of the objectives. This can be seen in fig. 5.3. The use of the 50x objective was found to deliver the clearest images of the BOP. Estimating the BOP's size involved taking two photographs with identical resolution: one focusing on the break-off point and the other on the transition from the refractive surface to the lens base. Using the known value of the lens width at this point, the size of the break-off point could be estimated. Estimating the height of the BOP proved difficult by just using the focal plane. This was addressed in 5.4.

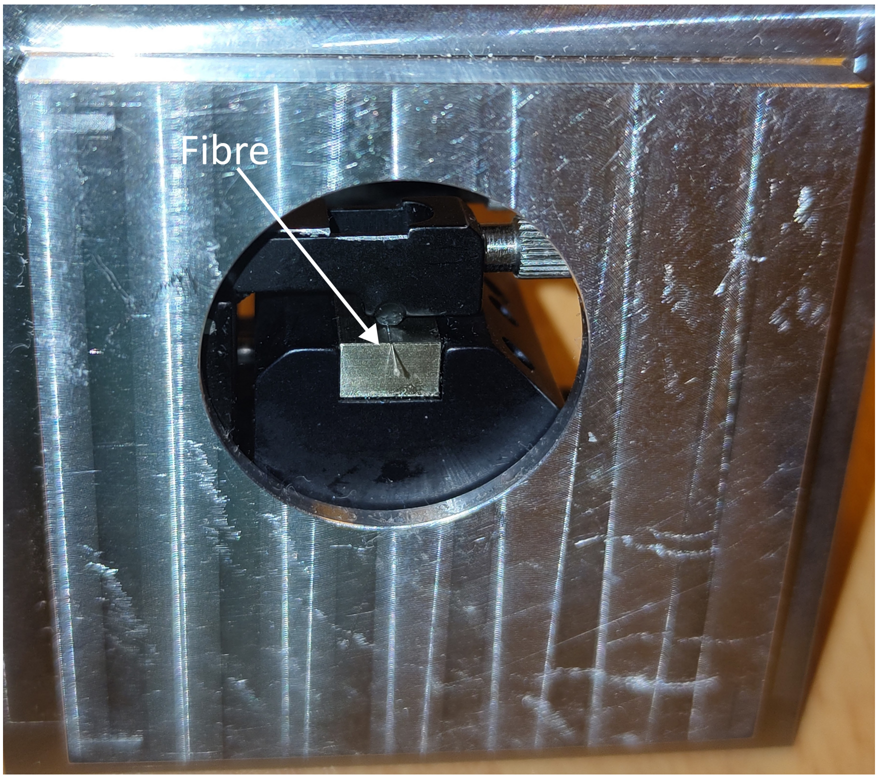

Figure 5.3: The fibre is placed in the fibre holder and the lens tip can be imaged using an inverted microscope.

5.3 Reducing Break-off Point size

In order to maximise the optical performance of the lens, the size of the BOP should be kept to a minimum or eliminated entirely and as such, numerous approaches have been examined.

5.3.1 Fibre Insertion

As previously discussed in subsec. 4.7.2, different approaches for inserting the fibre into the mask were explored. A comparison between approaches to attaching the OE to the fibre is shown in fig. 5.4, showing that the size of the break-off point has clear variations in size, depending on the technique used.

5.3.2 Chemical Approach

Attempts were made to dissolve the BOP using acetone and N-methyl-2-pyrrolidon (NMP). The OE was submerged in both chemicals for four 10 min intervals. Between each submersion, the BOP was

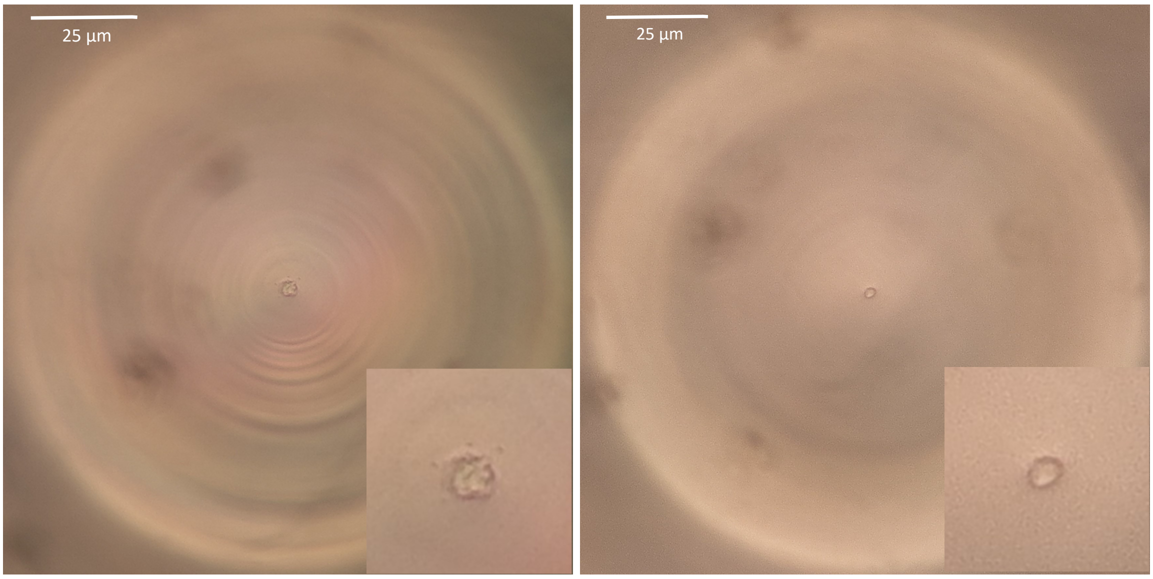

Figure 5.4: A comparison between the BOPs resulting from inserting fibre before loosening from the substrate (left) and inserting fibre after loosening. The estimated diameters of the BOPs are 6 µm for the left BOP and 4 µm for the right BOP. The ring-like structures seen on the left lens are a result of testing the hatching angle of the refractive surface and do not affect the shape of BOP.

observed. This attempt did not noticeably affect the BOP size, so this approach was not investigated further.

5.3.3 Plasma Cleaning

Using a plasma cleaner (Zepto, Diener electronic GmbH & Co. KG), multiple approaches were taken to test the effects of an oxygen gas plasma cleaning on the BOP. Initial attempts focused on observing the impact of plasma ashing on the structure of the OE. An OE, still attached to the substrate, was treated with plasma for 10 minutes at 40% power. Examination under the microscope revealed no signs of damage, confirming that the plasma ashing process does not harm the OE structure.

Subsequently, attempts were made to use the plasma cleaning process to erode the connection between the lower support and the lens. These tests involved an array of OEs exposed to multiple 3-minute cycles of ashing at 40% power. After each cycle, one of the OEs was attached to a fibre, with the aim of observing a reduction in the size of the BOP with increased cumulative plasma exposure. After a total of 18 minutes of plasma exposure, the connection point showed no signs of being removed. The slight variations in the size of the break-off point were likely due to the fibre insertion process rather than the plasma ashing.

The final method explored was plasma exposure of an OE that was already attached to a fibre. For this, the fibre was placed into a ferrule that kept the OE from touching the ground while in the plasma cleaner. Initial results after an exposure of 12 minutes at 40% power show marginal improvements, with the sharp edge of the BOP seemingly being reduced, as shown in fig. 5.5. A further test of 45 minutes at 40% power provided no usable measurements due to the OE disintegrating, likely due to the long exposure time.

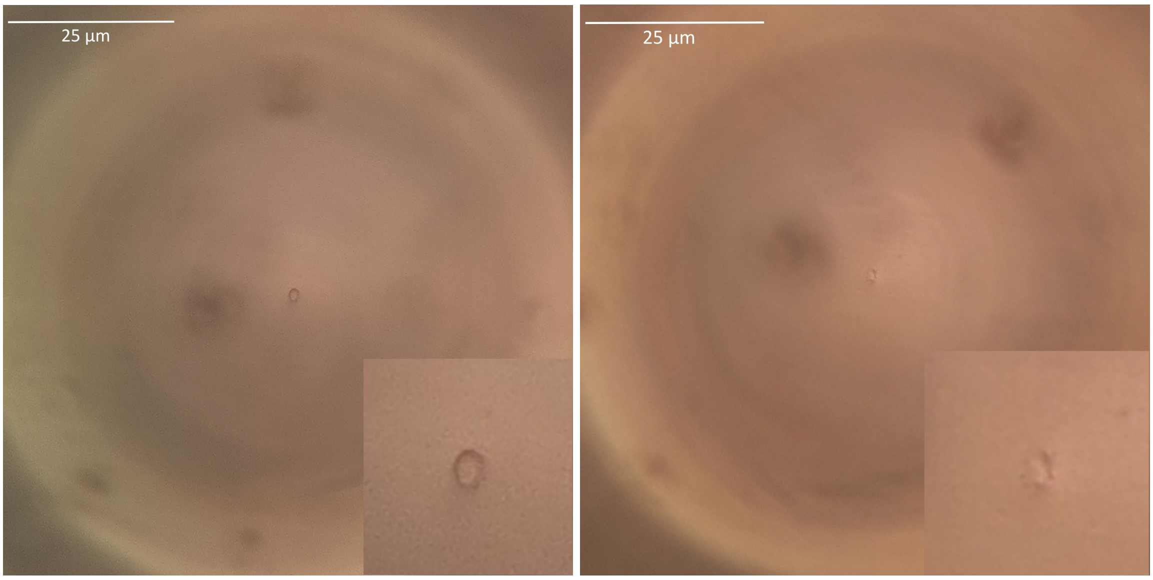

Figure 5.5: A comparison between the BOP of a lens on a fibre before (left) and after (right) being exposed to plasma cleaning at 40% power for 12 minutes. The left image has been rotated to allow for a better comparison of the BOPs. An image of the BOP magnified three times is inserted into each figure. Dark spots in images are artefacts resulting from the imaging process that were likely caused by dust on the objective or other imaging imperfections.

5.4 Interferometric Observations of Lens

In order to obtain a comprehensive view of the lens surface and the BOP, white light interferometry was conducted using a Mirau interferometer. This measurement process provides a highly detailed image of the lens surface by reconstructing its height profile by analysing interference patterns.

5.4.1 Measurement

The measurement was performed on OEs that had been exposed to plasma cleaning, in order to obtain a more detailed observation than the analysis using a microscope. OEs with different levels of plasma exposure were analysed. In the first measurement step, the stage tilt must be adjusted to ensure the OE is as perpendicular to the objective as possible. Even slight deviations can introduce minor errors in the accuracy of the analysed probe's shapes. Despite efforts to align the OE perfectly perpendicular, slight tilts may still occur and can be partially observed in the measurements. Once the tilt is set, the optimal zoom level is found through trial and error. Proper zoom adjustment is crucial, as the fringes of the measurement can become very noisy due to the lens's slope. The measurement is automated and is controlled through a GUI. This process must be repeated for each fibre analysed. The setup is shown in fig. A.4 and fig. A.6.

5.4.2 Analysis of Lens Surface

Figure 5.6 shows an example of a contour plot centred on the BOP, corresponding to a 41.25 µm × 41.25 µm window. The data corresponds to an OE that has been exposed to plasma for 12 minutes

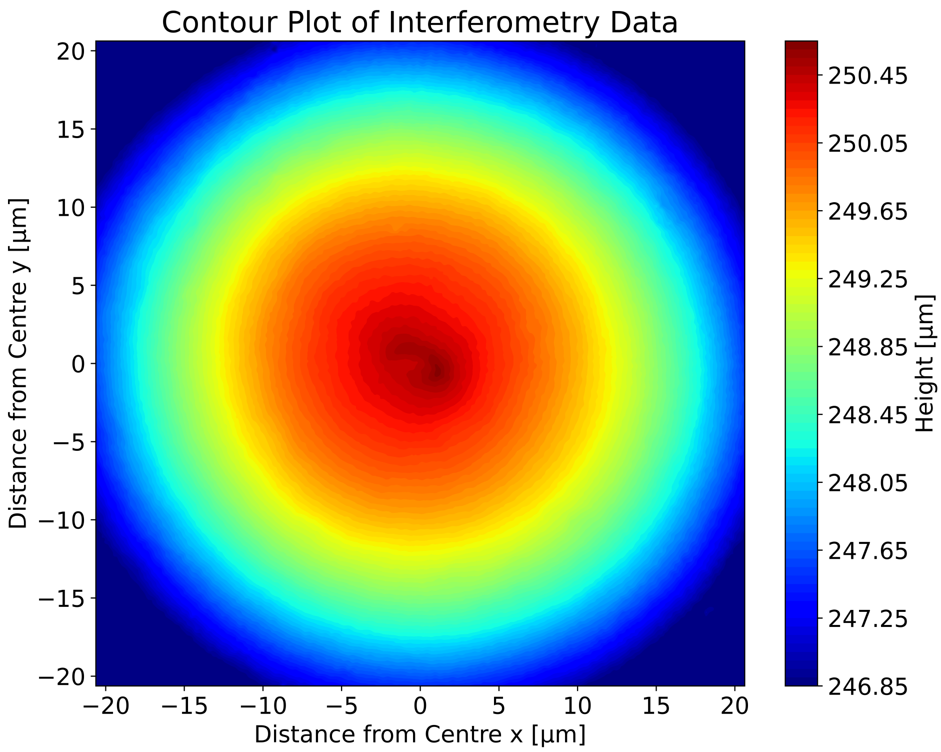

Figure 5.6: A contour plot of the lens tip from interferometry data. The smallest 5% of values, corresponding to noisy data in the corners, have been omitted. Closer inspection of BOP in fig. A.3

at 40% power. The surface of the lens can be compared to the programmed surface of the design. fig. 5.7 takes a side profile in both the x- and y-direction of the lens at the highest point of the BOP and compares it to the designed curve of the lens at that point. The side profiles are marked in fig. A.3 in white. Deviations under 500 nm are measured; this corresponds to a similar level of deviation measured by T. Gissibl et al. in [14].

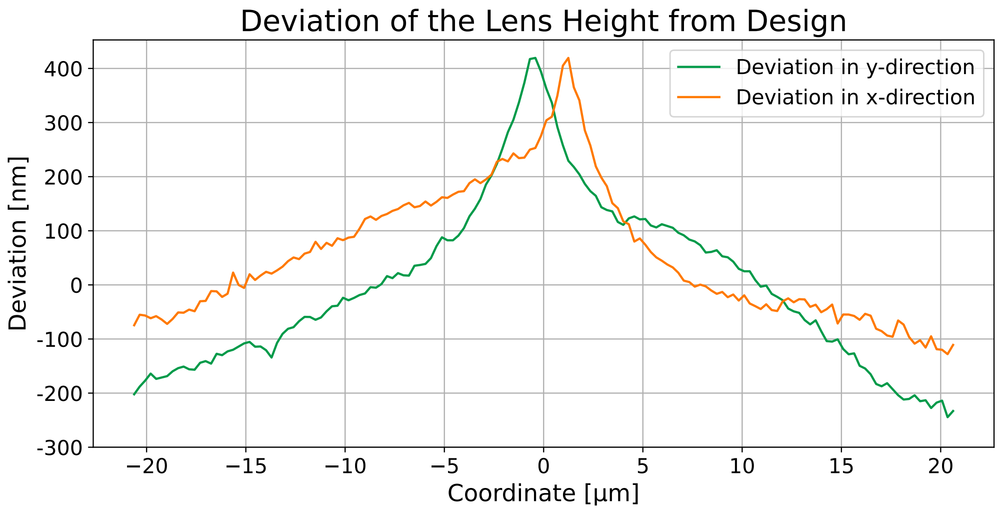

Figure 5.7: The deviation of the surface of the lens from the designed lens curve in the form of height profiles taken in the x- and y-direction from the maximum of the BOP. Corresponding profiles are shown in white in fig. A.3.

5.5 Analysis of Optical Performance

This section provides an overview of the experimental methods and setup used to measure the lens's performance.

5.5.1 Initial Observations

Initial observations of a beam passing through the OE were carried out by attaching the OE to a fibre with a patch connector on the other end and connecting the fibre to a fibre pen. The beam could then be imaged on a piece of white paper held a few centimetres from the lens to check if the beam was passing properly through the lens and allowed first comparisons to be made to the beam profile of a bare fibre attached to the fibre pen. The beam could also be imaged as it passed through the lens using a microscope, as seen in fig. 5.8.

5.5.2 Beam Profiling setup

The experimental setup used for analysing the beam profile is shown in fig. 5.9. The setup is based on similar setups that have been used in [49] and [50]. It comprises a 780 nm laser coupled into a single-mode fibre, with an OE attached to the other end. The fibre is mounted on a stage (MFA-CC, Newport Cooperation) that allows movement in three dimensions, controlled via a computer. The alignment of the stage can be adjusted using micrometre screws (not pictured). A camera (DCC1545M, Thorlabs Inc.) images the beam through a microscope. A photograph of the setup can be seen in fig. A.5

To image the beam profile, the camera captures images of the beam as the stage moves the fibre towards the microscope in the form of an intensity profile. With each step, a different part of the beam comes into focus, allowing a measurement of the beam width's dependence on the distance from the

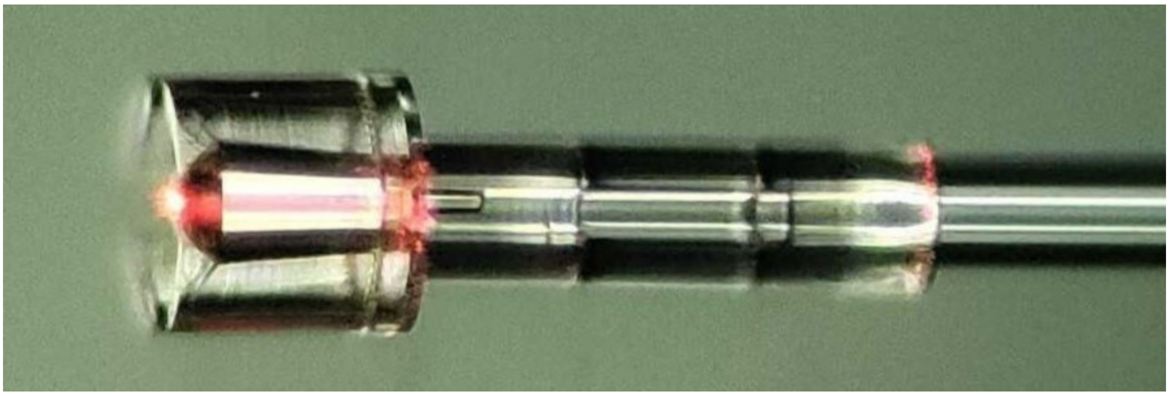

Figure 5.8: The beam from a laser pen passing through OE seen under a microscope. For scale, the fibre width is 125 µm.

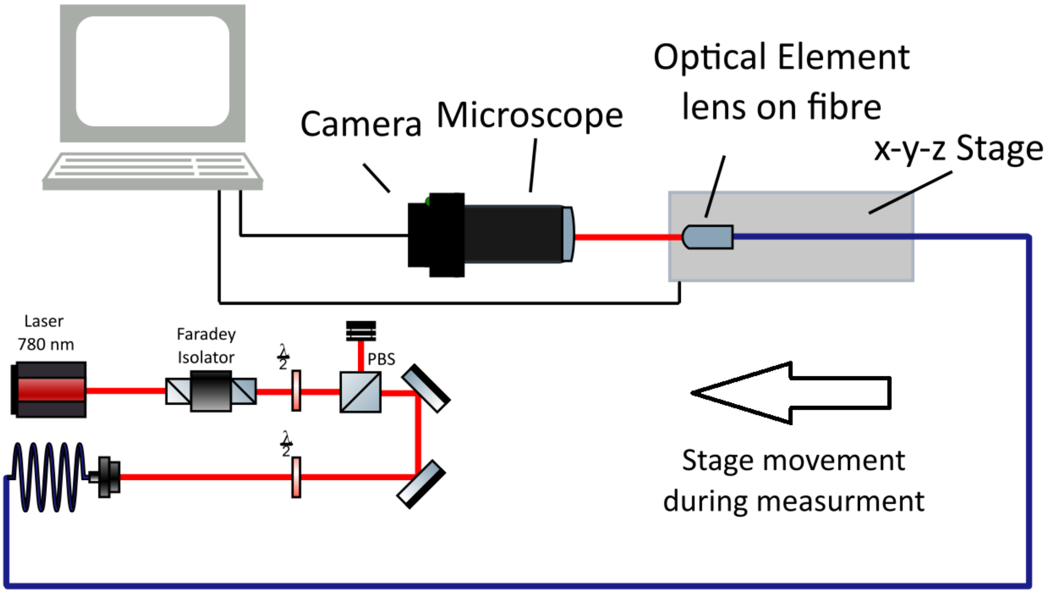

Figure 5.9: A diagram of the experimental setup used for profiling the beam.

lens. The beam width is determined by first fitting a 2D Gaussian profile to the measured intensity profile of the beam, centred around the intensity maximum. The fitted Gaussian profile's full width at half maximum (FWHM) is then used to determine the beam width in the x- and y-direction. An example of an intensity profile with the associated Gaussian fit is seen in fig. 5.10.

5.5.3 Notable Observations from Beam Profiling

During the observation of the beam profile, it was noticed that the beam's intensity profile could be elliptical, with differences in beam radii up to 15% being observed. Slight ellipticity is observed in the low-intensity regions of the beam seen in fig. 5.10. Attempts to mitigate the ellipticity through alignment of the fibre were unsuccessful, and it was observed that turning the fibre in its holder rotated

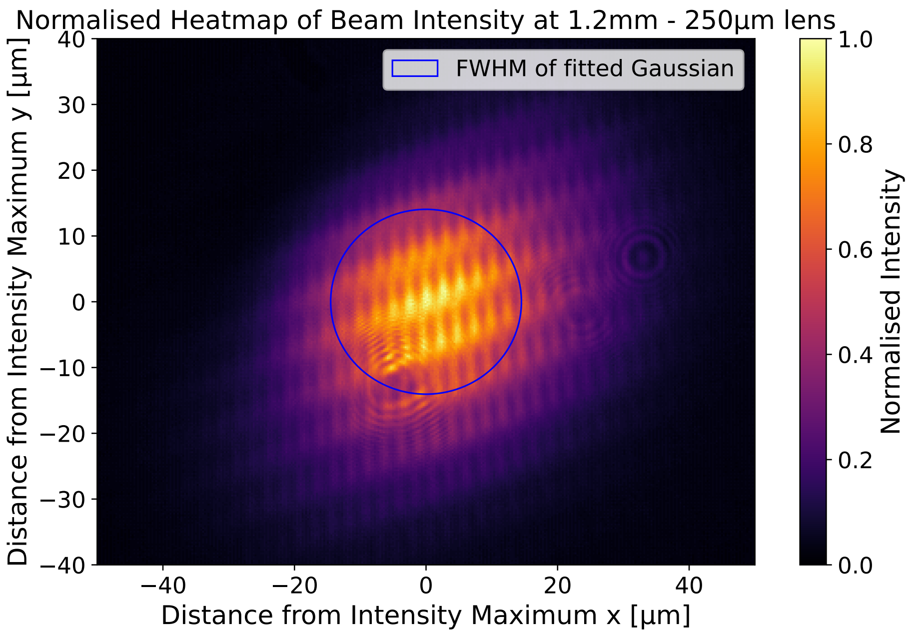

Figure 5.10: A normalised heat map of the beam from 250 µm lens at 1.2 mm from the lens. The FWHM of the fitted Gaussian distribution is shown in blue with an x-waist of 28.1 µm and a y-waist of 29.0 µm. The visible chequered-like structure in the image is an artefact of the camera.

the ellipse. It was concluded that the cause of the ellipse was either a problem with the lens itself or an issue with inserting the fibre. Using a single hatching angle for printing the lens base may contribute to the ellipse, so the use of "automatic hatch angle" could reduce the problem. A further cause may be an angle between the fibre and the base plate after inserting. This can be due to the cleave angle not being 90°, which could be avoided with prior inspection of the fibres. A further cause could be the misalignment of the fibre with the objective. Improvements in the alignment of the fibre with the microscope objective could also reduce the ellipticity.

5.5.4 Comparison of Lenses

The measurement of the beam profile was conducted on two types of lenses, the 250 µm lens with a ROC of −85.8 µm and a 136 µm lens with ROC of −53.5 µm. The 136 µm is designed to be un-optimised, with the total length being too short for the ROC, which is taken from the 150 µm lens from [45]. The beam divergence of a cleaved 780-HP fibre was also measured; this fibre was also used in combination with the lenses. It is important to note that even though the measurement program returns the FWHM of the beam, we use eq. (2.15) to convert the value to $w(z)$(eq. (2.12)) in order to determine the Rayleigh length.

Fig. 5.11 shows a comparison between the beam divergence of the 250 µm lens and the bare fibre over a distance of 950 µm. Figs. 5.12 to 5.15 show the beam radius $w(z)$ fitted to the four sets of beam divergence data. It should be noted that in the context of the collimating lens that z refers to the distance from the tip of the lens. In this case, the beam waist radius w_0 is the radius of the beam as it emerges from the lens.

The beam waist radius w_0 and Rayleigh length z_R are determined using the fitted curve. The values are shown in table 5.1. The beam divergence is calculated from the fit parameters. The experimentally measured value for the beam waist radius ($w_{0\,\mathrm{data}}$), corresponding to $w(z = 0)$, is used to calculate a Rayleigh length that can be compared to the fitted value. This comparison shows a deviation of around 140 µm for the 250 µm lens but a good match for the bare fibre. The deviation of the Rayleigh length for the lens could be due to the beam waist radius being measured at the wrong position, for example, within the lens itself, as determining the exact position of the tip of the lens can be difficult from just looking at the beam radius data alone. Still, it could be improved by adding an illumination source and taking a picture of the lens after each intensity measurement.

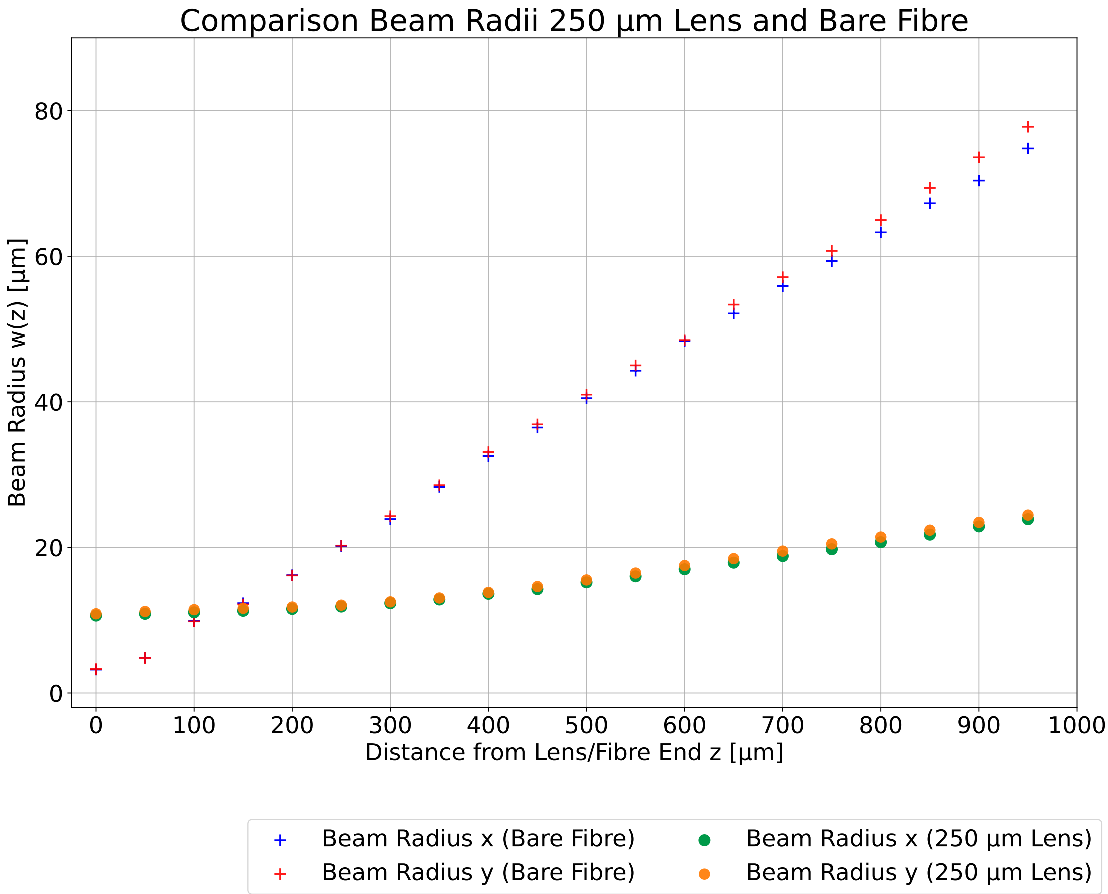

Figure 5.11: A plot comparing the beam radius $w(z)$ of a propagating beam emerging from a 250 µm lens and bare fibre z. Errors are too small to be seen in the plot.

The beam profile of an unoptimised 136 µm lens was tested. According to simulations using the ABCD matrix formalism by T. Gissibl (fig. 6.4 in [45]), the ideal ratio between the ROC and the total length is approximately 0.34. A simulation of a 250 µm lens with a ratio of about 0.4, as shown in fig. 6.3 in [45], results in an uncollimated linear beam profile. This same ratio of around 0.4 is achieved with a ROC of −53.5 µm combined with a total length of 136 µm. The beam propagation over a length of 1.6 mm, shown in fig. 5.16, matches the linear form predicted by the simulation. A linear regression fit was performed to verify the linear dependence of $w(z)$ on z.

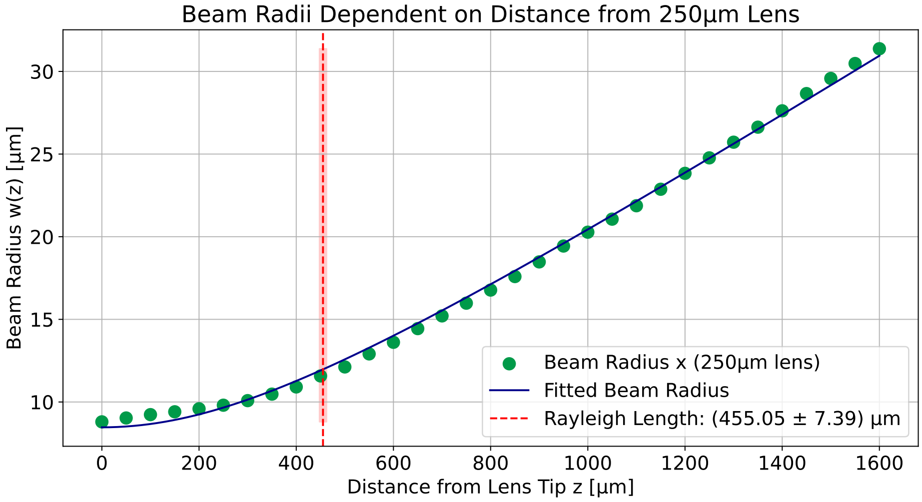

Figure 5.12: A plot comparing the horizontal beam radius $w(z)$ as a function of the distance from the tip of the 250 µm lens z. Fit performed using `scipy.optimise`. The Rayleigh length is included for visualisation purposes.

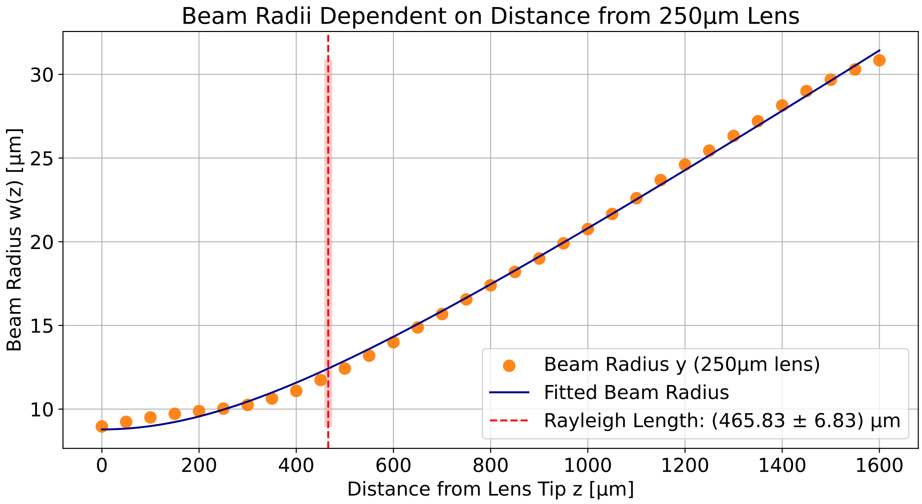

Figure 5.13: A plot comparing the vertical beam radius $w(z)$ as a function of the distance from the tip of the 250 µm lens z. Fit performed using `scipy.optimise`. The Rayleigh length is included for visualisation purposes.

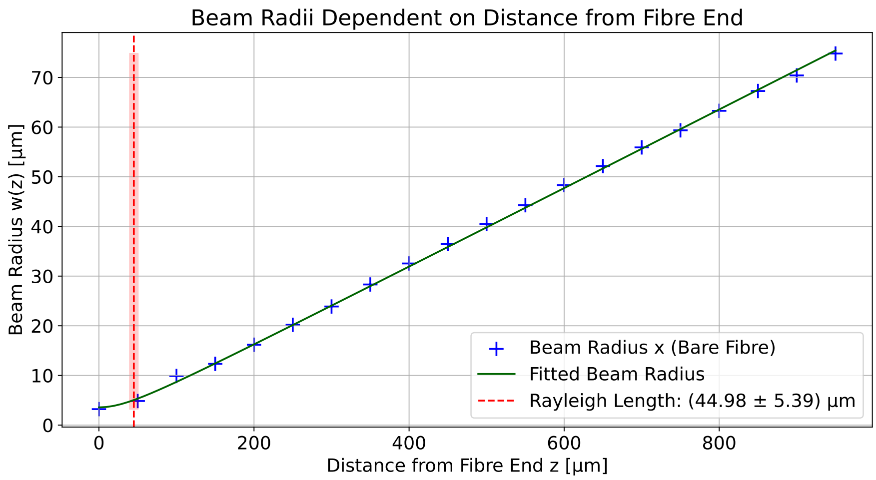

Figure 5.14: A plot comparing the horizontal beam radius $w(z)$ as a function of the distance from the tip of the bare fibre z. Fit performed using `scipy.optimise`. The Rayleigh length is included for visualisation purposes.

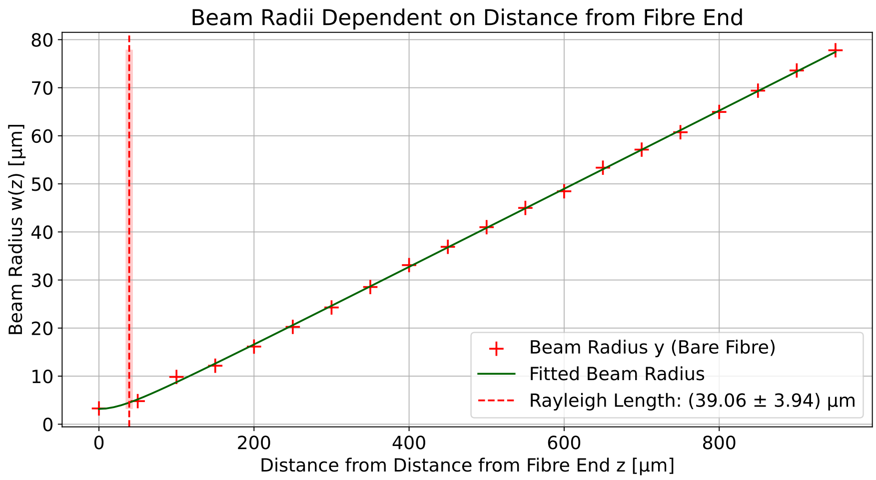

Figure 5.15: A plot comparing the vertical beam radius $w(z)$ as a function of the distance from the tip of the bare fibre z. Fit performed using `scipy.optimise`. The Rayleigh length is included for visualisation purposes.

Parameter	250 µm x	250 µm y	Bare fibre x	Bare fibre y
z_R[µm]	455.05	465.83	44.98	39.05
Δz_R[µm]	7.39	6.83	5.39	3.94
w_0[µm]	8.47	8.79	3.57	3.18
Δw_0[µm]	0.11	0.11	0.43	0.32
θ[mrad]	29.32	28.18	69.63	78.02
$\Delta\theta$[mrad]	1.90	1.77	4.19	3.93
$w_{0\,\text{data}}$[µm]	8.80	8.96	3.21	3.27
$z_{R\,\text{data}}$[µm]	311.90	323.35	41.50	43.06

Table 5.1: A table showing the different Gaussian parameters determined from the fitted data shown in figs. 5.12 to 5.15. All values correspond to fitted data unless specified.

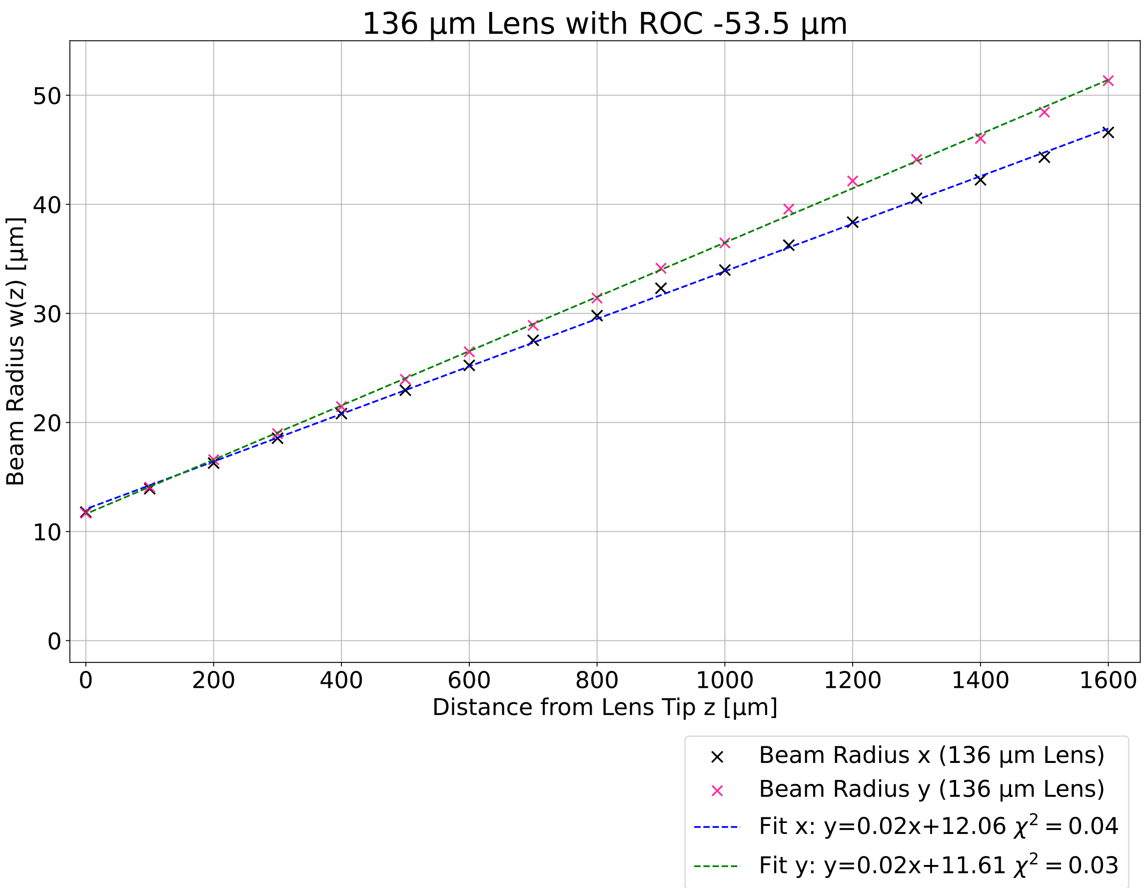

Figure 5.16: A plot of the beam radii of the 136 µm lens over a distance of 1.6 mm. Linear fit performed using `scipy. optimise`.

CHAPTER 6

Conclusion and Outlook

This thesis investigates a method for the scalable production of micro-optics for optical fibres using 3D printing via direct laser writing. Unlike traditional fibre-end printing techniques, this research focuses on printing an array of optical elements onto a glass substrate, which can then be attached to the end of a fibre.

The core objective is to develop a printing technique and design a structure to recreate existing lenses previously printed on fibre ends. This new approach simplifies the printing process by eliminating issues commonly encountered when printing directly onto the fibre end. Additionally, it increases the process's efficiency and scalability, allowing for printing multiple elements in a single print job.

This work uses existing collimating lenses as benchmarks, replicating them with identical printing parameters but in a different orientation. The developed method successfully prints collimating lenses with the same precision as the original on-fibre printing technique. Additionally, the versatility of the design and printing technique is demonstrated by its ability to accommodate lenses of various dimensions.

Attaching collimating lenses to fibre ends and aligning the fibre core with the lens centre involves using a mask connected to the top of the printed structure, into which the optical fibre is inserted. A method was developed that allows successful fibre insertion and detachment from the substrate.

Interferometry was utilised to analyse the printed lens surfaces for defects and to compare the printed surface with the designed surface. The deviation of the printed lens surface from the designed surface was less than 500 nm. The waist of a Gaussian beam emerging from the collimating lenses attached to single-mode fibres was also measured, demonstrating their optical performance and collimation over a distance of a few hundred micrometres.

In future experiments, one could integrate this approach to printing micro-optics with light extraction from known single photon sources such as quantum dots or hBN flakes. The method of printing the optics separate from the fibre could be utilised in the positioning of the optics above these photon sources. One could also investigate the printing of a fibre-to-fibre coupler using the collimating lenses successfully printed in this thesis.

APPENDIX A

Appendix

A.1 3D Printing of Lenses for Fibres

Additional photos to compliment chapter 4.

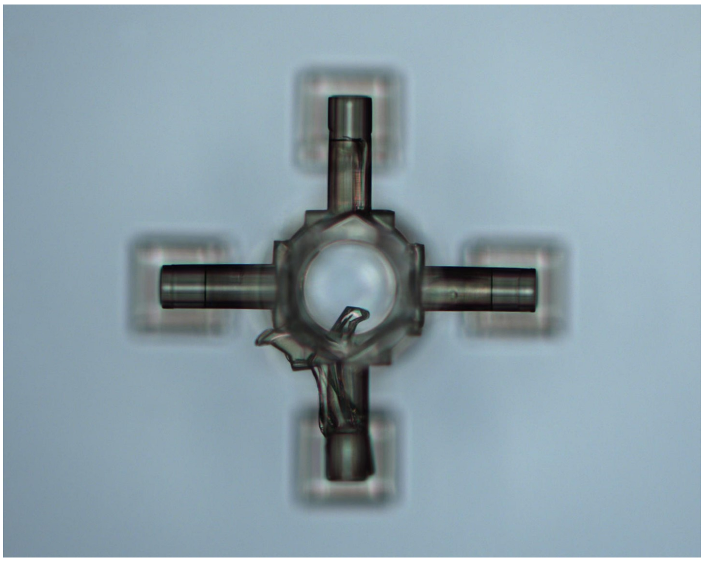

Figure A.1: A microscope image showing problems in the connection of the individual parts of the first design iteration of the OE.

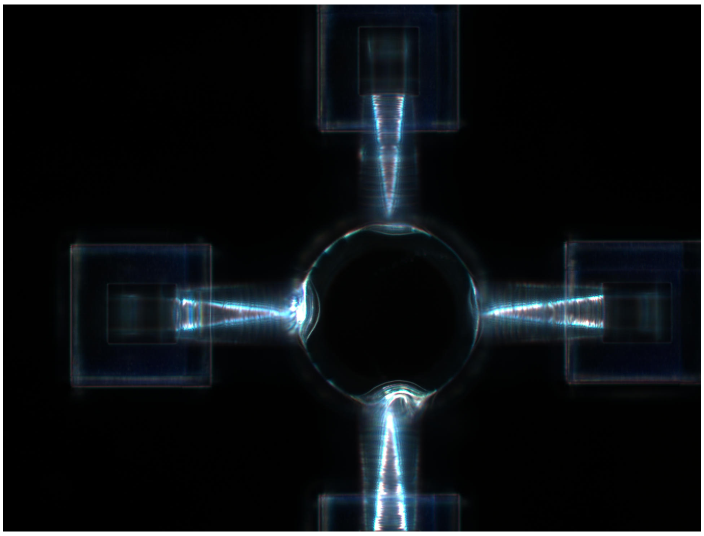

Figure A.2: A dark-field microscope image showing the deformation of the lens base due to the proximity effect in the first design iteration of the OE.

A.2 Experimental Methods and Results

Additional photos to compliment chapter 5.

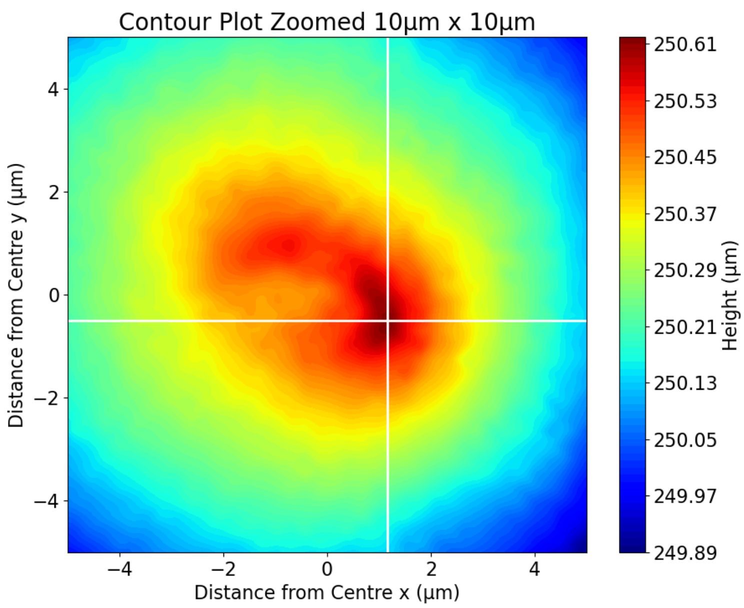

Figure A.3: A contour plot of the tip of the lens from interferometry data. The smallest 5% of values, corresponding to noisy data in the corners, has been omitted. White lines represent plotted row an column in fig. 5.7

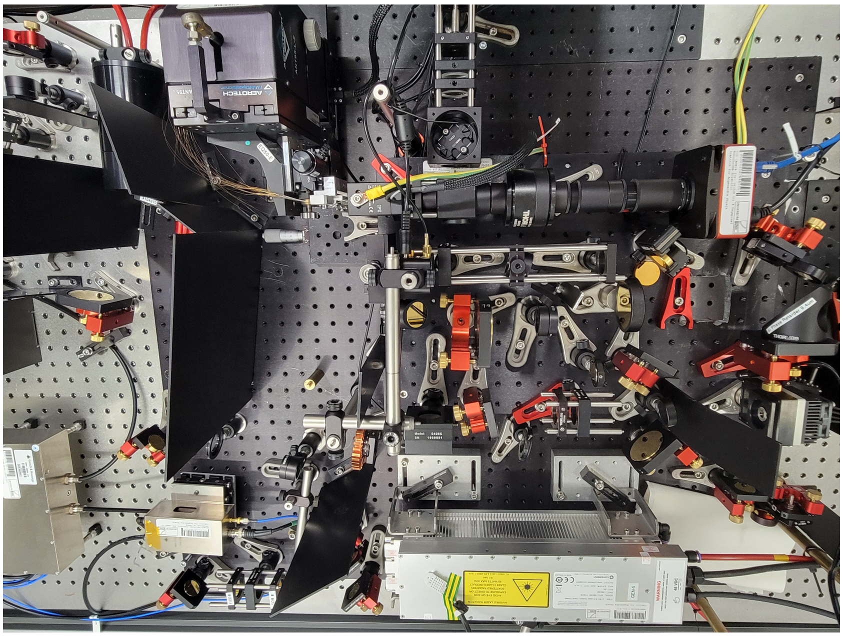

Figure A.4: A photograph of the interferometry setup. Photo by Paul Steinmann

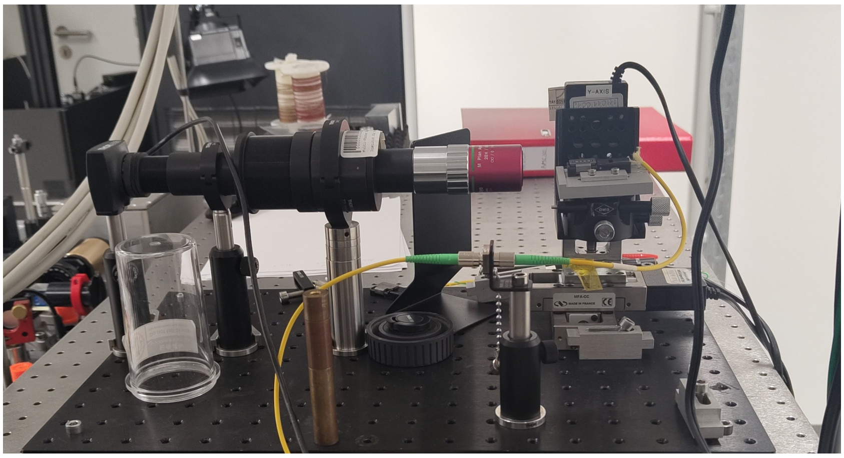

Figure A.5: A photograph of the microscope and stage of beam profiling setup

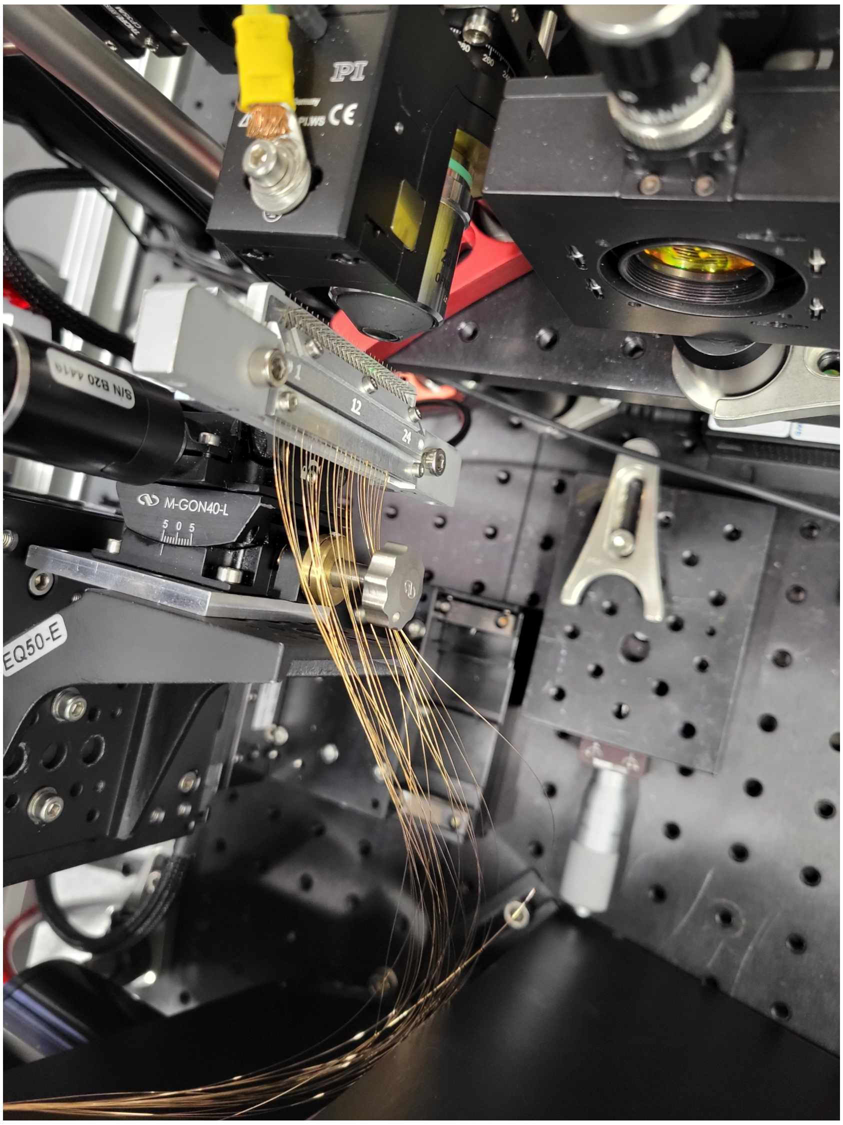

Figure A.6: A photograph of fibres being analysed in the interferometry setup. Photo by Paul Steinmann

Bibliography

[1] P. Steglich and F. D. Matteis, "Introductory Chapter: Fiber Optics", *Fiber Optics*, ed. by P. Steglich and F. D. Matteis, Rijeka: IntechOpen, 2019, chap. 1, URL: https://doi.org/10.5772/intechopen.85495 (cit. on p. 1).

[2] P. J. Winzer, D. T. Neilson and A. R. Chraplyvy, *Fiber-optic transmission and networking: the previous 20 and the next 20 years*, Opt. Express **26** (2018) 24190, URL: https://opg.optica.org/oe/abstract.cfm?URI=oe-26-18-24190 (cit. on p. 1).

[3] P. Rolfe, F. Scopesi and G. Serra, *Advances in fibre-optic sensing in medicine and biology*, Measurement Science and Technology **18** (2007) 1683 (cit. on p. 1).

[4] T. Udem, R. Holzwarth and T. W. Hänsch, *Optical frequency metrology*, Nature **416** (2002) 233 (cit. on p. 1).

[5] C. Marques, A. Leal-Júnior and S. Kumar, *Multifunctional integration of optical fibers and nanomaterials for aircraft systems*, Materials **16** (2023) 1433 (cit. on p. 1).

[6] R. Paschotta, *Fiber Bundles*, RP Photonics Encyclopedia, Available online at https://www.rp-photonics.com/fiber_bundles.html, URL: https://www.rp-photonics.com/fiber_bundles.html (visited on 13/06/2024) (cit. on p. 1).

[7] E. J. Seibel and Q. Y. Smithwick, *Unique features of optical scanning, single fiber endoscopy*, Lasers in Surgery and Medicine: The Official Journal of the American Society for Laser Medicine and Surgery **30** (2002) 177 (cit. on p. 1).

[8] C. M. Lee, C. J. Engelbrecht, T. D. Soper, F. Helmchen and E. J. Seibel, *Scanning fiber endoscopy with highly flexible, 1 mm catheterscopes for wide-field, full-color imaging*, Journal of biophotonics **3** (2010) 385 (cit. on p. 1).

[9] R. Paschotta, *Micro-optics*, RP Photonics Encyclopedia, Available online at https://www.rp-photonics.com/micro_optics.html, URL: https://www.rp-photonics.com/micro_optics.html (visited on 13/06/2024) (cit. on p. 1).

[10] W. Yuan, L.-H. Li, W.-B. Lee and C.-Y. Chan, *Fabrication of microlens array and its application: a review*, Chinese Journal of Mechanical Engineering **31** (2018) 1 (cit. on p. 1).

[11] D. Daly, R. Stevens, M. Hutley and N. Davies,
The manufacture of microlenses by melting photoresist,
Measurement Science and Technology **1** (1990) 759 (cit. on p. 1).

[12] R. Kirchner and H. Schift,
Thermal reflow of polymers for innovative and smart 3D structures: A review,
Materials Science in Semiconductor Processing **92** (2019) 58, Material processing of optical devices and their applications, ISSN: 1369-8001,
URL: https://www.sciencedirect.com/science/article/pii/S1369800118304761
(cit. on p. 1).

[13] Y. Luo et al., *Direct fabrication of microlens arrays with high numerical aperture by ink-jetting on nanotextured surface*, Applied Surface Science **279** (2013) 36, ISSN: 0169-4332,
URL: https://www.sciencedirect.com/science/article/pii/S0169433213006466
(cit. on p. 1).

[14] T. Gissibl, S. Thiele, A. Herkommer and H. Giessen,
Sub-micrometre accurate free-form optics by three-dimensional printing on single-mode fibres,
Nature Communications **7** (2016) 11763 (cit. on pp. 1, 19, 20, 25, 31, 38).

[15] *light (n.1)*, Oxford English Dictionary, December 2023,
URL: https://doi.org/10.1093/OED/1151812646 (cit. on p. 3).

[16] R. W. Boyd, *Nonlinear Optics*, 3rd ed., Academic Press, 2008, ISBN: 978-0-12-369470-6
(cit. on pp. 3, 4).

[17] E. Hecht, *Optics*, 4th international edition, International edition, Addison Wesley, 2002
(cit. on pp. 3, 6, 9).

[18] D. J. Griffiths, *Introduction to Electrodynamics*, Pearson, 2017, ISBN: 978-0-321-85656-2
(cit. on p. 4).

[19] N. Fatkullin et al., *Two-photon photopolymerization and 3D lithographic microfabrication*,
NMR• 3D Analysis• Photopolymerization (2004) 169 (cit. on p. 4).

[20] K. D. Belfield et al.,
Two-photon photochromism of an organic material for holographic recording,
Chemistry of materials **14** (2002) 3663 (cit. on p. 4).

[21] M. Rumi and J. W. Perry,
Two-photon absorption: an overview of measurements and principles,
Advances in Optics and Photonics **2** (2010) 451 (cit. on p. 4).

[22] J. V. Crivello and E. Reichmanis,
Photopolymer materials and processes for advanced technologies,
Chemistry of Materials **26** (2014) 533 (cit. on p. 5).

[23] J. Fischer et al.,
Three-dimensional multi-photon direct laser writing with variable repetition rate,
Optics express **21** (2013) 26244 (cit. on p. 5).

[24] K. Nakamura, *Photopolymers: photoresist materials, processes, and applications*,
CRC Press, 2018 (cit. on p. 6).

[25] X. He, L. Zang, Y. Xin and Y. Zou,
An overview of photopolymerization and its diverse applications,
Applied Research **2** (2023) e202300030 (cit. on p. 6).

[26] J.-P. Fouassier and J. Lalevée,
Photoinitiators for Polymer Synthesis: Scope, Reactivity, and Efficiency,
John Wiley & Sons, 2012 56 (cit. on p. 6).

[27] R. Paschotta, *Fibers*, RP Photonics Encyclopedia,
Available online at https://www.rp-photonics.com/fibers.html, 2005,
URL: https://www.rp-photonics.com/fibers.html (visited on 23/02/2024)
(cit. on p. 6).

[28] R. Paschotta, *Multimode Fibers*, RP Photonics Encyclopedia,
Available online at https://www.rp-photonics.com/multimode_fibers.html, URL:
https://www.rp-photonics.com/multimode_fibers.html (visited on 11/06/2024)
(cit. on p. 6).

[29] R. Paschotta, *Numerical Aperture*, RP Photonics Encyclopedia,
Available online at https://www.rp-photonics.com/numerical_aperture.html,
2007, URL: https://www.rp-photonics.com/numerical_aperture.html (visited on
23/02/2024) (cit. on p. 6).

[30] B. Mellish, *Singlemode fibre structure*, Accessed: 2024-06-03, Licensed under CC BY 4.0,
https://creativecommons.org/licenses/by/3.0/, Edited, 2007, URL:
https://commons.wikimedia.org/wiki/File:Singlemode_fibre_structure.svg
(cit. on p. 7).

[31] H. J. Eichler and J. Eichler, *Laser: Bauformen, Strahlführung, Anwendungen*, German,
Springer-Verlag, 2015 (cit. on pp. 7, 8).

[32] H.-A. Bachor and T. C. Ralph, *A guide to experiments in quantum optics*,
John Wiley & Sons, 2019 (cit. on p. 7).

[33] D. Meschede, *Optics, Light and Lasers: The Practical Approach to Modern Aspects of Photonics and Laser Physics*, 2, rev. enlarged ed., Wiley-VCH, 2008 (cit. on pp. 7–9).

[34] Edmund Optics, *Considerations in Collimation*, Accessed: 2024-06-11, 2024,
URL: https://www.edmundoptics.com/knowledge-center/application-notes/optics/considerations-in-collimation/ (cit. on p. 9).

[35] R. Paschotta, *Collimated Beams*, RP Photonics Encyclopedia,
Available online at https://www.rp-photonics.com/collimated_beams.html, URL:
https://www.rp-photonics.com/collimated_beams.html (visited on 11/06/2024)
(cit. on p. 9).

[36] A. Selimis, V. Mironov and M. Farsari,
Direct laser writing: Principles and materials for scaffold 3D printing,
Microelectronic Engineering **132** (2015) 83 (cit. on p. 11).

[37] M. T. Gale, *Fabrication of continuous-relief micro-optical elements by direct laser writing in photoresists*, Optical Engineering **33** (11 1994) 3556, ISSN: 0091-3286,1560-2303, URL: http://doi.org/10.1117/12.179892 (cit. on p. 11).

[38] V. Hahn, F. Mayer, M. Thiel and M. Wegener, *3-D laser nanoprinting*, Opt. Photonics News **30** (2019) 28 (cit. on p. 11).

[39] I. Bernardeschi, M. Ilyas and L. Beccai, *A review on active 3D microstructures via direct laser lithography*, Advanced Intelligent Systems **3** (2021) 2100051 (cit. on p. 11).

[40] S. Ruzin and H. Aaron, *1P vs 2P fluorescence imaging*, Accessed: 2024-06-13, URL: https://microscopy.berkeley.edu/2P/index.html (cit. on p. 12).

[41] N. G. C. KG, *NanoGuide*, Not accesable to public, URL: https://support.nanoscribe.com/hc/en-gb/ (visited on 25/05/2024) (cit. on pp. 11, 17).

[42] *Photonic Professional GT+ Operating Manual*, Document revision 597, Nanoscribe GmbH Co. KG, 2021 (cit. on p. 12).

[43] National Center for Biotechnology Information, *PubChem Compound Summary for CID 19042, Pentaerythritol triacrylate*, Year, URL: https://pubchem.ncbi.nlm.nih.gov/compound/Pentaerythritol-triacrylate (visited on 16/03/2024) (cit. on p. 14).

[44] A. Faßbender, *Adding New Functionalities to Optical Fiber Cavities by Direct Laser Writing*, Dissertation: Rheinische Friedrich-Wilhelms-Universität Bonn, 2023, URL: https://nbn-resolving.org/urn:nbn:de:hbz:5-73212 (cit. on pp. 14, 19, 20, 24, 30).

[45] T. Gissibl, *3D printing of sub-micrometer accurate ultra-compact free-form optics*, PhD thesis: University of Stuttgart, 2016, URL: http://dx.doi.org/10.18419/opus-10335 (cit. on pp. 19, 20, 22, 41, 42).

[46] S. K. Saha, C. Divin, J. A. Cuadra and R. M. Panas, *Effect of proximity of features on the damage threshold during submicron additive manufacturing via two-photon polymerization*, Journal of Micro-and Nano-Manufacturing **5** (2017) 031002 (cit. on p. 24).

[47] N. G. C. KG, *Advanced microoptics with 3D design freedom*, URL: https://www.nanoscribe.com/en/applications/additively-manufactured-3d-microoptics/ (visited on 05/05/2024) (cit. on p. 25).

[48] N. G. C. KG, *63x Objective*, Not accesable to public, URL: https://support.nanoscribe.com/hc/en-gb/articles/360002471754-63x-Objective (visited on 08/05/2024) (cit. on p. 27).

[49] D. Röser, *Fiber Fabry-Perot Cavities for Quantum Information and Spectroscopy*, Master's thesis: Rheinischen Friedrich-Wilhelms-Universität Bonn, 2019 (cit. on p. 39).

[50] M. Saravanan, *Mode-Matched Fiber Fabry-Pérot Cavities for Quantum Technologies*, Master's thesis: Rheinischen Friedrich-Wilhelms-Universität Bonn, 2020 (cit. on p. 39).

List of Figures

List of Tables

List of Abbreviations

1PA single-photon absorption

2PA two-photon absorption

CAD computer-aided design

D lens thicknesses

EM electromagnetic

GLW general writing language

GUI graphic user interface

IPA isopropanol

NA numerical aperture

OE optical element

PGMEA propylene glycol methyl ether acetate

PPTGT+ Photonic Professional GT+

ROC radius of curvature

STL stereolithography

Acknowledgements

First and foremost, I would like to thank Prof. Dr. Stefan Linden for suggesting the topic and for supervising my project over the last year. I also thank Prof. Dr. Sebastian Hofferberth for acting as a second corrector for this thesis.

I would also like to thank the entire Nanophotonics Group for making the past year very enjoyable. In particular, I would also like to thank Paul Steinmann for his help with the experimental setups along with his help proofreading of my thesis and informative discussions throughout the year. Special thanks also go to Hajo Schill and Anna Sidorenko for their feedback and corrections to my thesis. Thank you also to Alexander Faßbender and Lukas Tenbrake for their expertise on the Nanoscribe 3D printing system and for sharing their knowledge with me. Also, thank you to the entire Fiberlab team for their tips throughout the year.

Thank you also to Santhosh Surendra for his helpful feedback and the short-notice correction he made. Thank you to Dominic Schuh and Andreas Ulm for lending their perspective from outside the field of Optics on my thesis, along with Andy Lensch, Hannah Sieker, and Alwina for their support and for giving me some much-needed distractions throughout the last few weeks. A very special thank you goes to Maik Sarve for giving me his full support, even if it could not be done in person most of the time.

I also can not express my thanks to my dear friends and fellow master students Amélie Wagner and Frederick Ernst. All I can say to you is: we made it.

Finally, I would like to thank my parents, Mick and Gundula, my sister Maria and my brother Sam for their continued love and support. Last but not least, I want to thank Odontuya Aldar for always being there for me.